Structure and function of an intermediate GPCR-Gαβγ complex

Maxine Bi[1†], Xudong Wang[2†], Jinan Wang[3†], Jun Xu[4], Wenkai Sun[2], Victor Ayo Adediwura[3], Yinglong Miao[3*], Yifan Cheng[1,5*], Libin Ye[2,6*]

[1]Department of Biochemistry and Biophysics, University of California, San Francisco, CA 94143
[2]Department of Molecular Biosciences, University of South Florida, 4202 E Fowler Ave, Tampa, FL USA 33620
[3]Department of Pharmacology & Computational Medicinal Program, University of North Carolina at Chapel Hill, 116 Manning Drive, 11004C Mary Ellen Jones Building, Chapel Hill, NC 27599
[4]Department of Molecular and Cellular Physiology, Stanford University School of Medicine, Stanford, CA, USA
[5]Howard Hughes Medical Institute, University of California, San Francisco, CA 94143
[6]H. Lee Moffitt Cancer Center & Research Institute, 12902 USF Magnolia Drive, Tampa, FL, USA 33612

***Corresponding author**
Yinglong Miao, Associate Professor
Department of Pharmacology & Computational Medicinal Program, 116 Manning Drive, 11004C Mary Ellen Jones Building, Chapel Hill, NC 27599
E-mail: Yinglong_Miao@med.unc.edu Tel: 1-919-962-5696

Yifan Cheng, Professor
Department of Biochemistry and Biophysics, University of California, San Francisco, CA 94143; Howard Hughes Medical Institute, University of California, San Francisco, CA 94143
E-mail: Yifan.Cheng@ucsf.edu Tel: 1-415-514-9707

Libin Ye, Assistant Professor
Department of Molecular Biosciences, University of South Florida, 4202 E Fowler Ave, Tampa, FL, USA 33620; H. Lee Moffitt Cancer Center & Research Institute, 12902 USF Magnolia Drive, Tampa, FL, USA 33612
E-mail: libinye@usf.edu Tel: 1-813-974-6007

†: these authors contributed equally to this work.

Abstract

Despite hundreds of GPCR-Gαβγ complex structures, these snapshots uniquely capture the fully activated complex. Consequently, a comprehensive understanding of the conformational transitions during GPCR activation and the roles of intermediate complexes in signaling remain elusive. Guided by a conformational landscape profiled by ^{19}F quantitative NMR and Molecular Dynamics simulations, we engineered a mutant to trap an intermediate state of the adenosine A_{2A} receptor, allowing us to determine the structure of an unliganded GPCR-$G\alpha_s\beta\gamma$ intermediate complex and its functionality in signal transduction. We presented direct evidence that the GPCR intermediate forms a complex with $G\alpha_s\beta\gamma$ and initiates a rate-limited nucleotide exchange without progressing to the fully activated end-state complex, thereby bridging a critical gap in our understanding the complexity of GPCR signaling, including efficacy and selectivity.

Maintex

G protein-coupled receptors (GPCRs) are the largest family of human membrane proteins, encompassing over 800 distinct members. Due to their vital roles in various (patho)physiological processes, significant efforts have been made to unravel their activation mechanisms, aiming to modulate therapeutic signaling with precision. Recent advancements, especially in single-particle cryo-electron microscopy (cryo-EM), have facilitated the structural determination of hundreds of GPCR-Gαβγ complex since 2017(*1-3*). These complex structures uniquely represent the receptors in their fully activated end-states. Yet, the GPCR signaling process is more intricate than what these structures alone can depict. Multiple studies have shown that GPCR activation entails transitions through several intermediate complexes, including two critical steps pre-coupled and partially activated intermediate GPCR-G protein complexes (Fig. 1A) (*4-12*). Isolating such transient complexes to study their signaling roles presents a significant challenge.

Using the adenosine-A_{2A} receptor (A_{2A}R) as a model system and applying ^{19}F quantitative NMR (^{19}F-qNMR), we mapped the conformational landscape of this GPCR in response to ligand actions. Within this landscape, we identified two transient active-like intermediates (S3 and S4) that are positioned between the inactive (defined as S1 and S2) and the fully activated states (S5)(*13*) (Fig.1A). Among these conformations, S1 and S2 have been defined by crystal structures (*14, 15*), and the S5 state has been characterized by cryo-EM (PDB ID: 6GDG)(*16*) (Fig. 1A and Fig. S1). The structures of S3 and S4 in complex with G proteins, however, remain uncharacterized. With the R291A point mutation, which we previously determined to lock the A_{2A}R into the intermediate S4 state (Fig. 1)(*13*), we have continued to investigate the structure and function of this intermediate state in complex with G protein in this study. Our study seeks to answer questions such as whether the intermediate S4 can directly interact with and regulate G protein without transitioning to the S5 state and how the G protein responds to the intermediate S4. Understanding the structural and functional roles of individual intermediate GPCR-G protein complexes will significantly advance our knowledge at the molecular mechanistic level regarding the signaling efficacy, bias, and allostery, which is pivotal for improving drug designs(*5, 17, 18*).

S4 state binds to $G\alpha_s\beta\gamma$ and initiates nucleotide exchange

We first examined whether the WT*-R291A mutant, which is trapped in the S4 state, can bind to the $G\alpha\beta\gamma$. Here, the S4 trapped mutant was introduced to a previously defined construct ($A_{2A}R$-316-V229C, denoted as WT*),(*13*) and we referred to WT*-R291A simply as R291A. We incubated ^{19}F-labeled R291A with $G\alpha\beta\gamma$, subjected it to ^{19}F-NMR, and measured the linewidth of the NMR resonance. Indeed, we observed a linewidth broadening for the S4 resonance compared to the receptor alone, suggesting direct binding of $G\alpha\beta\gamma$ to $A_{2A}R$ in the S4 state (Fig. S2A). This was further confirmed by a complex band of apo R291A-$G\alpha_s\beta\gamma$ in native-PAGE (Fig. S2B).

Next, we assessed how the S4 regulates G protein function by performing nucleotide hydrolysis, binding, and exchange assays. As shown in Fig. 2A, the R291A mutant-mediated GTP hydrolysis from the G protein occurred at a much slower rate compared to the full agonist-bound WT*-$G\alpha_s\beta\gamma$ (representing the S5-$G\alpha_s\beta\gamma$). However, the addition of full, partial, or inverse agonists did not alter the GTP hydrolysis level substantially in the R291A mutant. This ligand-independent hydrolysis behavior is in stark contrast to the wild-type construct, where ligand binding dramatically changes the hydrolysis level(*19, 20*). To further investigate the reduced hydrolysis level, we measured the initial rates and Michaelis constants of GTP hydrolysis. The initial rate of GTP hydrolysis mediated by R291A was only one-twentieth of that mediated by NECA-bound WT* (Fig. 2B), while the Michaelis constant exhibited a similar pattern (Fig. 2C).

We proposed a simple model to explain the limited GTP hydrolyzing capacity of the S4-mediated G protein, where nucleotide binding to G protein is a two-step process. A nucleotide GTP initially binds to a site with low affinity and hydrolysis (site1) in the intermediate S4-G protein complex. Upon the transitioning from S4 to S5, the G protein changes its conformation to allow the GTP to access the site 2, the canonical nucleotide-binding site. We tested this model by examining the binding of BODIPY-FL-GDP (Figs. 2D and 2H). The BODIPY-FL-GDP bound to the NECA-bound WT*-mediated G protein exhibited a higher K_D than that of the R291A-mediated G protein, although both reached equilibrium at 1.5 hrs. For the R291A-mediated G protein, a secondary association event was observed after 1.5 hrs with a K_D value 10 times lower, which was not the case observed in the NECA-bound WT*. We attribute this difference to the restricted accessibility of the site 2, caused by spatial constraints resulting from the partially open AHD domain in the S4-mediated G-protein, while this site is freely accessible in the S5-mediated G-protein. A similar pattern was noted in BODIPY-FL-GTP binding assays, where BODIPY-FL-GTP showed more efficient binding to the S5-mediated G protein with a higher K_D value (Figs.2E and 2H). The spatial limited association process was also evident in BODIPY-FL-GTP-γ-S (Fig. 2F) in both S5- and S4-mediated G protein because the BODIPY head was linked to γ-phosphate, which is meant to be inserted into the site 2. The bulky BODIPY head insertion restricted exchange and hydrolysis. Titration of GTP into the BODIPY-FL-GDP equilibrium system led us to conclude that the S4-mediated G protein has a reduced nucleotide exchange rate compared to the S5-mediated G protein (Fig. 2G). A previous study of β_2AR indicated that GDP release occurs much faster than the formation of fully activated complex(*21*), while MD simulations suggested that GDP is released when the $G\alpha_s$ is not fully opened(*22*). Collectively, our data suggests the

intermediate S4-mediated G-protein initiates nucleotide exchange before transitioning to the fully activated S5 state, albeit at a reduced rate.

Structure of the ligand-free intermediate S4-mini-G$\alpha_s\beta\gamma$ complex

Building upon the two-step nucleotide binding model, we hypothesized that the intermediate S4 state not only adopts a conformation distinct from the S5 but also binds to the G protein in a manner conformationally different from the S5-bound state. To test this hypothesis and enhance our understanding of the molecular mechanisms involved, we aimed to determine the structure of the intermediate S4 state in complex with the G protein.

To capture the structure of intermediate S4 state in complex with G proteins, we assembled a stable complex by incubating the R291A mutation with mini-Gα_s, known as mini-Gα_s399, and the Gα_s-stabilizing nanobody, NB35, in conjunction with Gβ1γ2. As evidenced by ^{19}F-qNMR, the receptor preserves the conformation of the S4 state in complex with G proteins (Figs. 1B and 1C). We determined a cryo-EM structure of this S4-mini-G$\alpha_s\beta\gamma$ complex at a 2.8 Å resolution, revealing the key interaction sites between A_{2A}R and mini-G$\alpha_s\beta\gamma$ without ligand (Figs. 1D-F and Fig. 3A). For a comprehensive understanding of our methods, we have detailed the sample preparation, cryo-EM data acquisition, and processing steps in Figs. S3-6, and Table S1.

Comparisons of the S4-mini-G$\alpha_s\beta\gamma$ complex with the S5-mini-G$\alpha_s\beta\gamma$ complex (PDB ID: 6GDG), as depicted in Supplementary videos 1 and 2, reveal key differences between the two states. The extracellular orthosteric binding pocket of the intermediate complex S4-mini-G$\alpha_s\beta\gamma$ is less compact than of the S5-mini-G$\alpha_s\beta\gamma$ (Fig. 3B), yet more constricted compared to the inactive state(*14, 15*). Transitioning from the inactive to the intermediate state S4 involves significant inward movements of all domains relative to TM1 in the extracellular domains. The shift from the intermediate to the fully activated complex results in observable movements of these domains. This is consistent with the ^{19}F-qNMR study, which recorded a substantial chemical shift (~400 Hz) when the receptor transitioned from the inactive states S1-2 to intermediate S4, while the shift from S4 to S5 resulted in a minor chemical shift (~60 Hz) (Fig. 3F). Closer inspection of the TM6 domain, using the ^{19}F-tag labeling site as a reference, revealed a clockwise rotation consistent with the ^{19}F-qNMR resonance, where the NMR signal for the S4 state is at a lower field than the S5 state. Indeed, the conformation of the intermediate S4 state is on the trajectory from the inactive S1-2 to the fully activated S5 states.

One of the key microswitches in the receptor is the $\underline{P^{5.50}I^{3.40}F^{6.44}}$ motif, which is a crucial hydrophobic switch between TM5, TM3 and TM6 and is implicated in receptor activation(*1, 23*). In the fully activated receptor, $P^{5.50}$ and $F^{6.44}$ are in cis positions, forming a strong CH-π interaction(*24*), and the CH_3 group of $I^{3.40}$ also forms a robust CH_3-π interaction with $F^{6.44}$, stabilizing the fully activated conformation. In contrast, these interactions are weakened in the S4-mini-G$\alpha_s\beta\gamma$ complex because $P^{5.50}$ and $I^{3.40}$ are oriented away from $F^{6.44}$ (Fig. 3D). Another key microswitch is the $\underline{CW^{6.48}xP}$ motif, where $P^{6.50}$ acts as a hinge in TM6 and facilitates the opening of the cytoplasmic cavity during activation(*25*). Our cryo-EM structure clearly shows $P^{6.50}$ in an “intermediate” position, bridging the inactive

and active states (Fig. 3E). The third microswitch, the NPxxY$^{7.53}$ on TM7, along with a conserved tyrosine Y$^{5.58}$ in TM5, stabilizes the receptor's active state(*26-28*). As illustrated in Fig. 3G, a strong H-bond is observed between Y$^{5.58}$ and Y$^{7.53}$ in the S5-mini-G$\alpha\beta\gamma$ complex. This interaction draws Y$^{5.58}$ on TM5 closer to TM7, maintaining the compactness of the TM bundle in the S5-G protein complex, as shown in the animation from the S4-mini-G$\alpha_s\beta\gamma$ transitioning to the S5-mini-G$\alpha\beta\gamma$ (Supplementary videos 1 and 2). Therefore, transitioning from the S4- to the S5-mini-G$\alpha_s\beta\gamma$ strengthens the H-bond interaction as Y$^{5.58}$ moves closer to the TM7 domain, aiding in the insertion of the G protein into the cavity. Our analysis indeed supports the idea that the S4 conformation can regulate G protein signaling to some degree without transitioning to the fully activated S5 state.

Next, we examined the interfacial interaction between Cα5 helix of mini-Gα_s (Fig. 3C) and the transmembrane bundle comprising TM3, TM6 and TM7 domains - critical components in regulating G protein nucleotide exchange. As highlighted in Fig. 3C, the S4-mini-G$\alpha_s\beta\gamma$ adopts a slightly more open conformation than the S5-mini-G$\alpha_s\beta\gamma$. The Cα5 helix is significantly rotated outward and retracted from the G protein-binding pocket, accompanied by the disengagement of the αN helix of the Gα_s protein from the H8 helix of the receptor. This retraction measures approximately 2 Å and the rotation is at a 2° spinal clockwise angle from the S5-mini-G$\alpha_s\beta\gamma$. This motion is further detailed in Fig. 3E, which shows the primary interactions at the junction composed of TM3, TM6, TM7 domains, and the Cα5 segment from mini-Gα_s. During the activation process, the clockwise rotation of TM6 and counterclockwise rotation of Cα5 culminate in a compact end-state complex. The transition from the S4- to the S5-mini-G$\alpha_s\beta\gamma$ entails a further insertion of the G protein and an inward rotation of the receptor domain, evidenced by the formation of the salt bridge R$^{7.56}$-E392$^{G\alpha}$ and the cation-π interaction between R$^{7.56}$ and H$^{6.32}$, coupled with a strengthened cation-π interaction between R$^{3.50}$ and Y391$^{G\alpha}$. However, the R$^{7.56}$ to A$^{7.56}$ mutation eliminates this interaction.

Molecular basis of A_{2A}R function in the S4 state

To validate the conformational transition between the S4 and S5 states, we applied all-atom Gaussian accelerated MD (GaMD) simulations, starting from atomic structure of the S5-mini-G$\alpha_s\beta\gamma$ complex (6GDG) with a R291A mutation modeled in silico. Indeed, the R291A mutation facilitated transition of the 6GDG structure (S5 state, Fig.1B) to an energy minimum conformation that closely matches our new cryo-EM structure. We refer to this as cS4 state, where "c" stands for computational model, and here the Cα5 helix in Gα_s retracted from the receptor by ~2 Å. The center-of-mass distance between the receptor NPxxY motif and the last five residues of Cα5 helix increased from ~13.2 Å in the "S5" state to ~15.3 Å in the "cS4" state (Fig. 4A and Fig. S7). As a control, GaMD simulations showed that the cWT*-mini-G$\alpha_s\beta\gamma$ complex remained stable, mainly sampling one low-energy state, corresponding to the S5 (Fig. 4B). These simulations independently validated the conformation of the intermediate S4 state determined from single particle cryo-EM.

Furthermore, we performed additional GaMD simulations to examine GDP release. In the cS5-G$\alpha_s\beta\gamma$ system, GDP was observed moving away from the initial binding site by up to

~12 Å repeatedly (Fig. 4C). In contrast, GDP underwent significantly smaller movements up to only ~8 Å in the cS4-G$\alpha_s\beta\gamma$ system (Fig. 4F). Free energy calculations also indicated a "GDP Released" state in the cWT*-G$\alpha_s\beta\gamma$ system and only a "Partially Released" state in the R291A-G$\alpha_s\beta\gamma$ system (Figs. S8A-C), where the AHD domain of Gα_s transitioned from the "Open" to "Partially Open" conformation, with the orientation angle between the AHD and Ras-like domain decreasing to ~30° (Figs. S8D-E) (*1, 29*). Together, these observations suggest that the S4 state mediated G protein has a reduced capacity for GDP release compared to the S5 state, aligning with the nucleotide exchange data shown above.

A limited nucleotide exchange model for intermediate GPCR-G$\alpha_s\beta\gamma$ complex

A mechanistic model is proposed to understand the rate-limited nucleotide exchange in the intermediate GPCR-G protein complex (Fig. 5). The transition from the intermediate to the fully activated complex involves a conformational change at the interface, where the TM6 helix of the receptor rotates clockwise by 8° while the Cα5 helix from the Ras-like domain rotates anticlockwise by 2°. This leads to a more compact interaction between the receptor and G protein, coupled with a 2 Å uplift of the Cα5 helix. This uplift results in the disengagement of the H1 from the Cα5 helix, facilitating the separation of AHD domain from Ras-like domain and thereby exposing the bound GDP at site 2. Simultaneously, this process assists the relocation of GTP from site 1 to site 2, replacing GDP. However, in the S4-mediated G protein, the substitution of $R^{7.56}$ with alanine ($A^{7.56}$) results in the loss of both the intramolecular cation-π ($R^{7.56}$-$H^{6.32}$) interaction and the intermolecular salt bridge ($R^{7.56}$-$E392^{G\alpha}$). Instead, a partially opened AHD domain is seen (Fig. 4E), which can be attributed to a weak electrostatic H-bond (Q59-T369, 4 Å)(*30*) between Cα5 and H1 helices. While in the closed state of the AHD domain, an additional CH_3-π interaction between F376 and M60 plays a significant role (Fig. 4D and Figs. 4G-I). Of note, in all complex structure resolved so far, the crystallographic complex structure of β2AR-G$\alpha\beta\gamma$ represents the sole fully activated complex structure, in which the AHD domain with an open of 88° while all others are between 55-65°. This could be the effect from crystallographic packing in the crystallization process (*31*). Collectively, these findings provide a molecular basis for the limited nucleotide exchange observed in the intermediate GPCR-G protein complex.

Discussion

Previous MD simulation has indicated that GTPγS and GDP exhibited different contact patterns with G protein(*32*). A recent study also indicated a transition process of nucleotide by titrating GTP into a β_2AR-regulated G protein from a "loose" interaction site to the canonical nucleotide-binding pocket by 2 Å, deduced from a G$\alpha\beta\gamma$ dissociation event from a fully activated complex (*31*). Our study provides evidence for a 2 Å distance dislocation of nucleotide, regulated by a "lift" of the Cα5 tail by 2 Å, which is essential for dislodging the AHD domain of the G protein from the Ras-like domain. This facilitates the opening of the canonical site 2, accommodating GTP for free-nucleotide exchange and hydrolysis(*33*). However, the precise location of site 1 en route from the S4-G$\alpha\beta\gamma$ to the S5-G$\alpha\beta\gamma$ in the GPCR activation process and its specific functional role in G protein signaling remain unclear and require further characterization in the future.

GPCR activation is known to involve the transition through multi-states(*4-12*). However, transient intermediate states represent higher energy substates from energy landscape perspective and are thus challenging to characterize, especially with regard to obtaining transient GPCR-G protein complexes and studying their functions. Our current study demonstrates a strategy whereby intermediate conformational states can be identified by ^{19}F-qNMR, trapped by point mutation, and structurally and functionally characterized in their complexes with G proteins. Although we used $A_{2A}R$ as a model system, it is clear that such strategy of utilizing^{19}F-qNMR-guided cryo-EM, in which 19F-NMR serves as conformational indicator, can be broadly applied to study transient complexes of other GPCRs and proteins of interest during activation or inhibition processes. Deciphering the functions of intermediate states and their complexes enables a comprehensive understanding of GPCR signaling complexity and the exploration of alternative therapeutic approaches by targeting a specific disease-related conformation(complex). As the advance of our knowledge on structures and functions of individual conformational states and their complexes, it will become possible to design drug based on their conformational selectivity on the receptor, considering signaling bias originated from conformational bias (*5*).

309 **Figures**

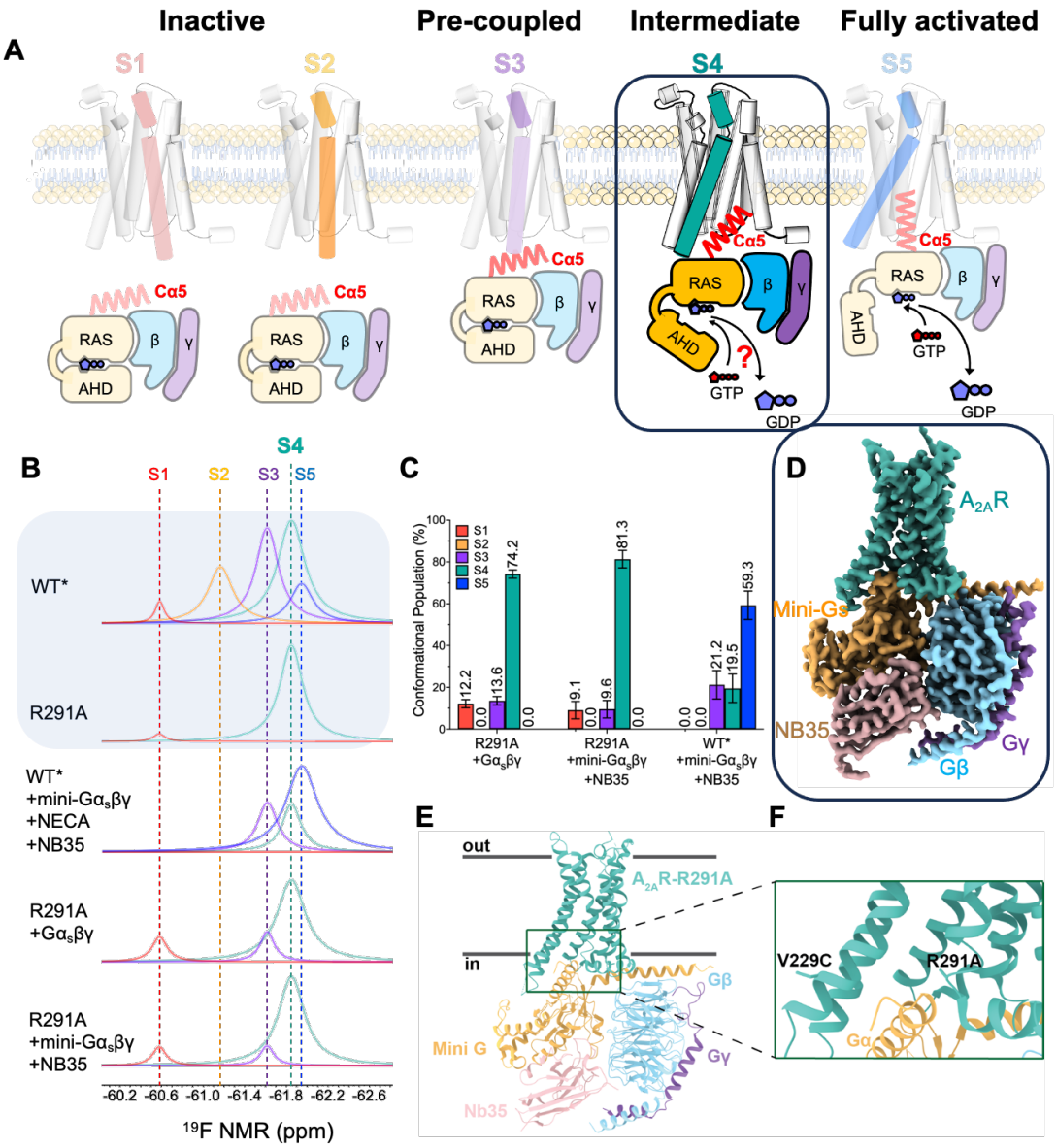

Fig. 1. Identification of the intermediate complex investigated in this study. (A) Proposed activation model of GPCR, including inactive states S1 and S2, pre-coupled complex (S3-G$\alpha_s\beta\gamma$), intermediate complex (S4-G$\alpha_s\beta\gamma$), and the fully activated complex (S5-G$\alpha_s\beta\gamma$), in which S4-G$\alpha_s\beta\gamma$ was highlighted in teal for this study. **(B)** In reference to Fig. S1, the deconvoluted conformational profiles probed by ^{19}F-qNMR for the R291A construct were presented as a function of G$\alpha_s\beta\gamma$ and mini-G$\alpha_s\beta\gamma$. ^{19}F-qNMR spectra of WT* and R291A were used as the benchmarks for S1 through S5, adapted from the reference (gray box, Wang et al, 2023, Nature Commun). The spectrum of WT*+mini-G$\alpha_s\beta\gamma$+NECA+NB35 represents the feature for PDB: 6GDG. **(C)**The population distributions of conformational states for R291A+mini-G$\alpha_s\beta\gamma$+NB35, R291A+G$\alpha_s\beta\gamma$, and WT*+mini-G$\alpha_s\beta\gamma$+NB35 (S5-G$\alpha_s\beta\gamma$). The SD values were determined based on spectral S/Ns and fitting errors of the deconvolutions. **(D)** Ribbon representation of S4-mini-G$\alpha_s\beta\gamma$. **(E)** Highlighted interfacial section of S4-mini-G$\alpha_s\beta\gamma$. **(F)** cryo-EM density map of intermediate S4-mini-G$\alpha_s\beta\gamma$ complex.

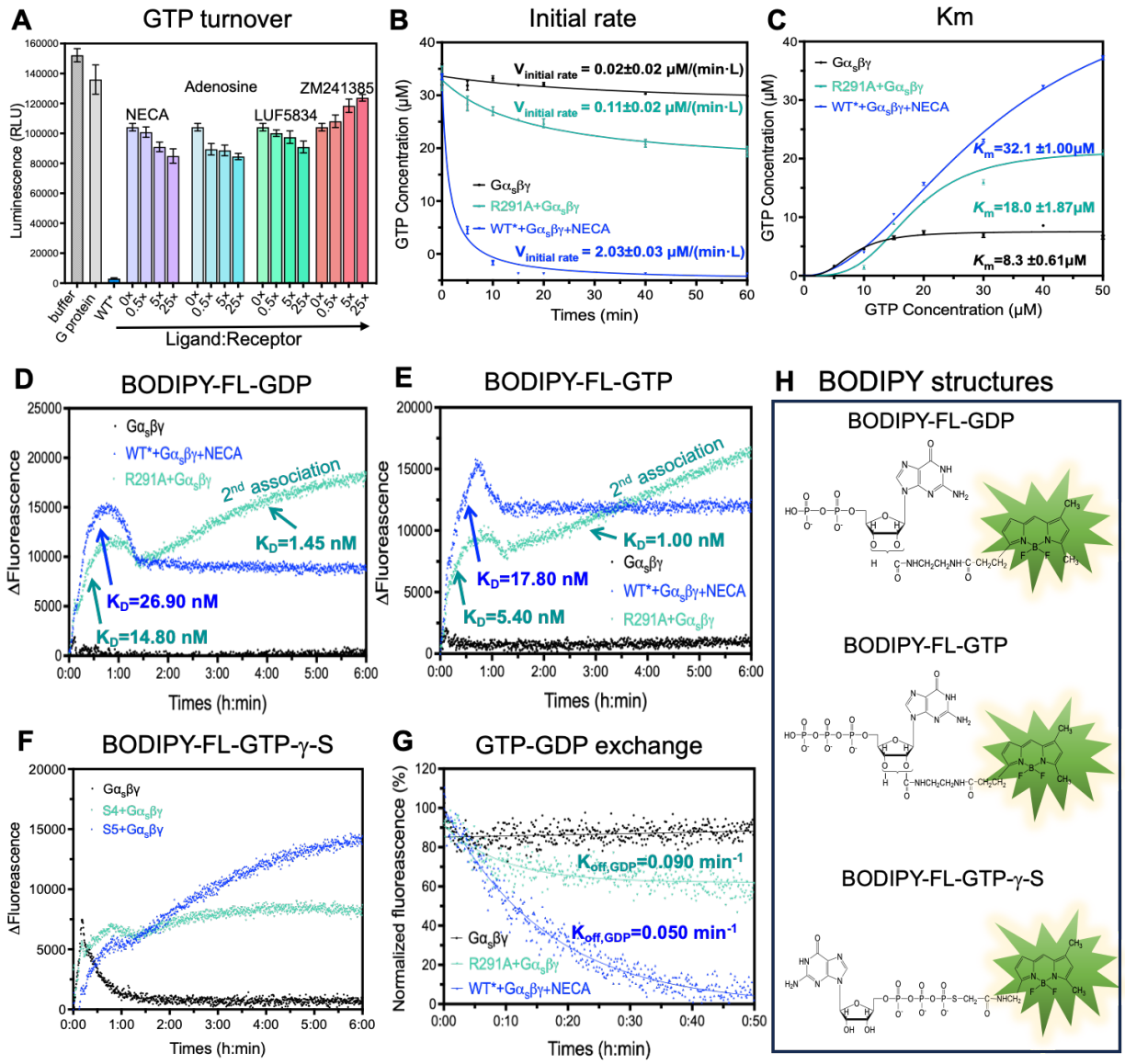

Fig. 2. S4-mediated GTP hydrolysis and nucleotide exchange. (A) GTP hydrolysis of the S4-mediated $G\alpha_s\beta\gamma$ as a function of inverse, partial, and full agonists, in reference to $G\alpha_s\beta\gamma$ alone (negative control) and the S5-mediated $G\alpha_s\beta\gamma$ (positive control). **(B)**Time course of GTP hydrolysis of the S4-mediated $G\alpha_s\beta\gamma$, in reference to $G\alpha_s\beta\gamma$ alone (negative control) and the S5-mediated $G\alpha_s\beta\gamma$ (positive control); the initial rate of each catalysis was also calculated as presented. **(C)** Km values for S4-mediated $G\alpha_s\beta\gamma$, in reference to $G\alpha_s\beta\gamma$ alone (negative control) and the S5-mediated $G\alpha_s\beta\gamma$ (positive control). **(D)** BODIPY-FL-GDP binding assay. **(E)** BODIPY-FL-GTP binding assay. **(F)** BODIPY-FL-GTP-γ-S binding assay **(G)** GTP-GDP exchange rate comparison. **(H)** The structures of BODIPY-FL-GDP, BODIPY-FL-GTP, and BODIPY-FL-GTP-γ-S.

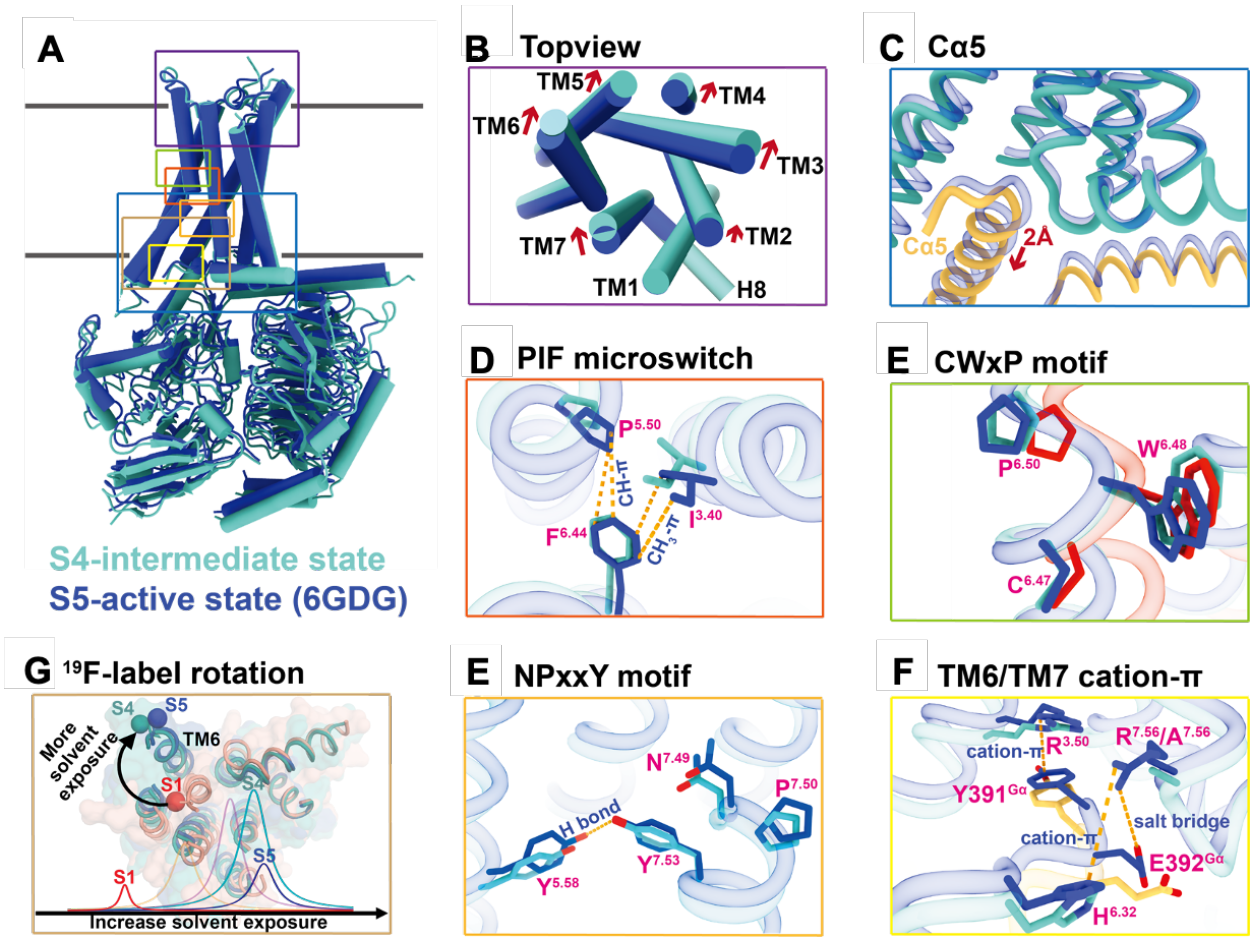

Fig. 3. Structural features of the receptor in intermediate complex. (A) Superimposed cylinder representations of S4-mini-G$\alpha_s\beta\gamma$ and S5-mini-G$\alpha_s\beta\gamma$. **(B)** Top view of ligand binding domain of the S4 state compared to the S5 state. **(C)** Cα5 motion of Gα_s. **(D)** PIF microswitch. **(E)** CWxP motif. **(F)** ^{19}F-tag rotation, and corresponding NMR spectrum. **(G)** NPxxY motif. **(H)** TM6 and TM7 cation-π interaction in two complexes.

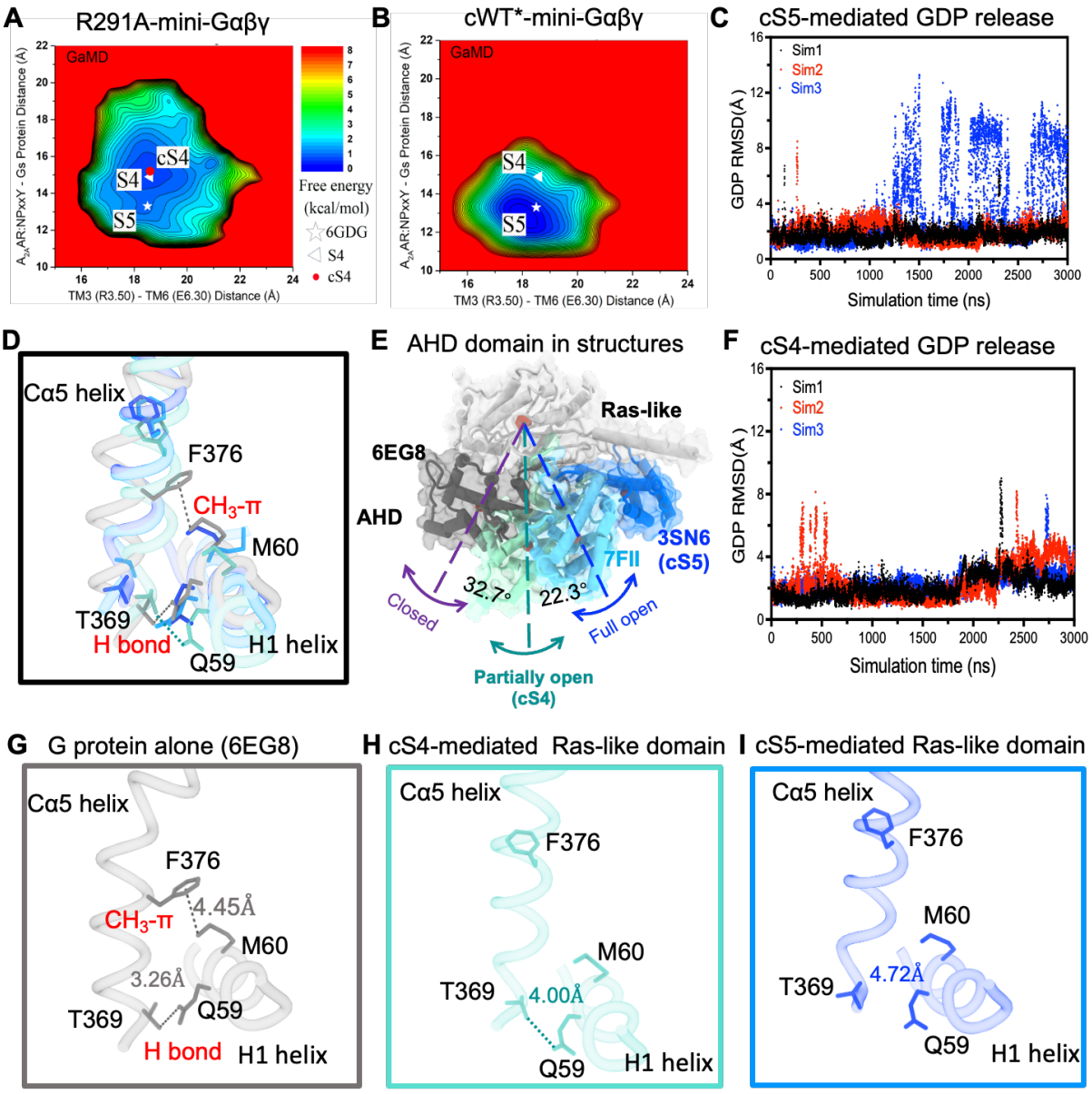

Fig. 4. Structural features of $A_{2A}R$ and G protein in GaMD simulation/structures. (A) 2D free energy profiles of the cR291A-mini-G$\alpha_s\beta\gamma$ complex system. **(B)** 2D free energy profiles of the cWT*-mini-G$\alpha_s\beta\gamma$ complex systems. The white triangle and asterisk indicate cryo-EM structures of the S5 and S4 states, respectively. **(C)** Root-mean square deviation (RMSD) of GDP relative to the initial position in the GaMD simulation for cS5-mediated G protein. **(D)** Superimposed positions of Cα5 and H1 helices when G protein is inactive, partial activated, and fully activated. **(E)** The positions of AHD domain when G protein is inactive, partial activated, and fully activated. **(F)** RMSD of GDP relative to the initial position in the GaMD simulation for cS4-mediated G protein. (**G-I**), The relative positions of Cα5 and H1 helices when G protein is inactive (6EG8), partial activated (cS4-mediated), and fully activated (cS5-mediated).

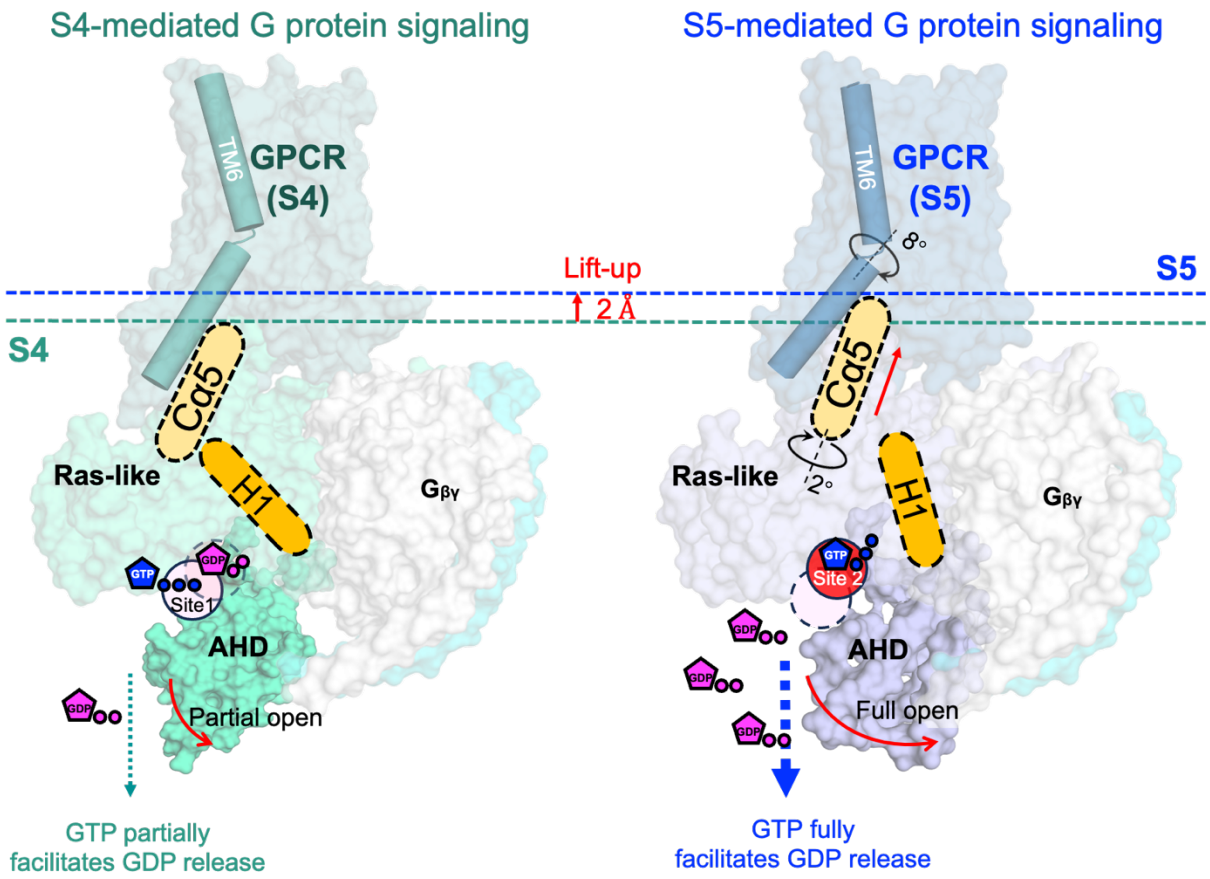

Fig. 5. A rate-limited nucleotide exchange model for intermediate GPCR-G$\alpha_s\beta\gamma$ complex. In the S5-mediated Gα the interaction between Cα5 and H1 helices was interrupted while this interaction is partially maintained through a weakened H-bond between Cα5 and H1 helices in Ras-like domain.

References

1. S. G. Rasmussen *et al.*, Crystal structure of the beta2 adrenergic receptor-Gs protein complex. *Nature* **477**, 549-555 (2011).
2. L. Ye, X. Wang, A. McFarland, J. J. Madsen, (19)F NMR: A promising tool for dynamic conformational studies of G protein-coupled receptors. *Structure* **30**, 1372-1384 (2022).
3. Y. Zhang *et al.*, Cryo-EM structure of the activated GLP-1 receptor in complex with a G protein. *Nature* **546**, 248-253 (2017).
4. D. Hilger, The role of structural dynamics in GPCR-mediated signaling. *FEBS J* **288**, 2461-2489 (2021).
5. X. Wang, A. McFarland, J. J. Madsen, E. Aalo, L. Ye, The potential of (19)F NMR application in GPCR biased drug discovery. *Trends Pharmacol Sci* **42**, 19-30 (2021).
6. L. Heo, M. Feig, Multi-state modeling of G-protein coupled receptors at experimental accuracy. *Proteins*, (2022).
7. L. Ye, N. Van Eps, M. Zimmer, O. P. Ernst, R. S. Prosser, Activation of the A_{2A} adenosine G-protein-coupled receptor by conformational selection. *Nature* **533**, 265-268 (2016).
8. L. Ye, A. P. Orazietti, A. Pandey, R. S. Prosser, High-efficiency expression of yeast-derived G-protein coupled receptors and (19)F labeling for dynamical studies. *Methods Mol Biol* **1688**, 407-421 (2018).
9. D. M. Perez, S. S. Karnik, Multiple signaling states of G-protein-coupled receptors. *Pharmacological reviews* **57**, 147-161 (2005).
10. M. Marti-Solano, D. Schmidt, P. Kolb, J. Selent, Drugging specific conformational states of GPCRs: challenges and opportunities for computational chemistry. *Drug discovery today* **21**, 625-631 (2016).
11. S. S. Dong, W. A. Goddard, 3rd, R. Abrol, Identifying multiple active conformations in the G protein-coupled receptor activation landscape using computational methods. *Methods in cell biology* **142**, 173-186 (2017).
12. S. Madurga, M. Nedyalkova, F. Mas, J. L. Garces, Ionization and conformational equilibria of citric acid: delocalized proton binding in solution. *The journal of physical chemistry. A* **121**, 5894-5906 (2017).
13. X. Wang, C. Neale, S. K. Kim, W. A. Goddard, L. Ye, Intermediate-state-trapped mutants pinpoint G protein-coupled receptor conformational allostery. *Nat Commun* **14**, 1325 (2023).
14. A. S. Dore *et al.*, Structure of the adenosine A2A receptor in complex with ZM241385 and the xanthines XAC and caffeine. *Structure* **19**, 1283-1293 (2011).
15. V. P. Jaakola *et al.*, The 2.6 angstrom crystal structure of a human A2A adenosine receptor bound to an antagonist. *Science* **322**, 1211-1217 (2008).
16. J. Garcia-Nafria, Y. Lee, X. Bai, B. Carpenter, C. G. Tate, Cryo-EM structure of the adenosine A(2A) receptor coupled to an engineered heterotrimeric G protein. *Elife* **7**, (2018).
17. T. Kenakin, New concepts in pharmacological efficacy at 7TM receptors: IUPHAR review 2. *Br J Pharmacol* **168**, 554-575 (2013).
18. J. P. Mahoney, R. K. Sunahara, Mechanistic insights into GPCR-G protein interactions. *Curr Opin Struct Biol* **41**, 247-254 (2016).

19. S. K. Huang *et al.*, Allosteric modulation of the adenosine A(2A) receptor by cholesterol. *Elife* **11**, (2022).
20. S. K. Huang *et al.*, Delineating the conformational landscape of the adenosine A(2A) receptor during G protein coupling. *Cell* **184**, 1884-1894 e1814 (2021).
21. Y. Du *et al.*, Assembly of a GPCR-G protein complex. *Cell* **177**, 1232-1242 e1211 (2019).
22. C. Bai *et al.*, Exploring the Activation Process of the beta2AR-Gs Complex. *J Am Chem Soc* **143**, 11044-11051 (2021).
23. D. Wacker *et al.*, Structural features for functional selectivity at serotonin receptors. *Science* **340**, 615-619 (2013).
24. N. J. Zondlo, Aromatic-proline interactions: electronically tunable CH/pi interactions. *Acc Chem Res* **46**, 1039-1049 (2013).
25. L. Shi *et al.*, Beta2 adrenergic receptor activation. Modulation of the proline kink in transmembrane 6 by a rotamer toggle switch. *J Biol Chem* **277**, 40989-40996 (2002).
26. L. Ragnarsson, A. Andersson, W. G. Thomas, R. J. Lewis, Mutations in the NPxxY motif stabilize pharmacologically distinct conformational states of the alpha(1B)- and beta(2)-adrenoceptors. *Sci Signal* **12**, (2019).
27. V. Cherezov *et al.*, High-resolution crystal structure of an engineered human beta2-adrenergic G protein-coupled receptor. *Science* **318**, 1258-1265 (2007).
28. G. H. Westfield *et al.*, Structural flexibility of the G alpha s alpha-helical domain in the beta2-adrenoceptor Gs complex. *Proc Natl Acad Sci U S A* **108**, 16086-16091 (2011).
29. J. Duan *et al.*, Structures of full-length glycoprotein hormone receptor signalling complexes. *Nature* **598**, 688-692 (2021).
30. G. A. J., An introduction of Hydrogen bonding. *Oxford Unviersity Press*, (1998).
31. M. M. Papasergi-Scott *et al.*, Time-resolved cryo-EM of G-protein activation by a GPCR. *Nature*, (2024).
32. T. Flock *et al.*, Universal allosteric mechanism for Galpha activation by GPCRs. *Nature* **524**, 173-179 (2015).
33. R. O. Dror *et al.*, SIGNAL TRANSDUCTION. Structural basis for nucleotide exchange in heterotrimeric G proteins. *Science* **348**, 1361-1365 (2015).
34. W. Zhao, X. Wang, L. Ye, Expression and purification of yeast-derived GPCR, Gα and Gβγ subunits for structural and dynamic studies. *Bio Protoc* **11**, e3919 (2021).
35. B. Carpenter, C. G. Tate, Engineering a minimal G protein to facilitate crystallisation of G protein-coupled receptors in their active conformation. *Protein Eng Des Sel* **29**, 583-594 (2016).
36. B. Carpenter, C. G. Tate, Expression and purification of mini G proteins from Escherichia coli. *Bio-protocol* **7**, e2235-e2235 (2017).
37. S. Mondal, K. Hsiao, S. A. Goueli, A homogenous bioluminescent system for measuring GTPase, GTPase activating protein, and guanine nucleotide exchange factor activities. *Assay Drug Dev Technol* **13**, 444-455 (2015).
38. J. N. Wang *et al.*, Gaussian accelerated molecular dynamics: Principles and applications. *Wires Comput Mol Sci* **11**, e1521 (2021).

39. Y. Miao, V. A. Feher, J. A. McCammon, Gaussian Accelerated Molecular Dynamics: Unconstrained Enhanced Sampling and Free Energy Calculation. *Journal of Chemical Theory and Computation* **11**, 3584-3595 (2015).
40. A. Waterhouse *et al.*, SWISS-MODEL: homology modelling of protein structures and complexes. *Nucleic Acids Res* **46**, W296-W303 (2018).
41. Q. Hu, K. M. Shokat, Disease-Causing Mutations in the G Protein Gαs Subvert the Roles of GDP and GTP. *Cell* **173**, 1254-1264.e1211 (2018).
42. K. Vanommeslaeghe, A. D. MacKerell, CHARMM additive and polarizable force fields for biophysics and computer-aided drug design. *Biochimica et Biophysica Acta (BBA) - General Subjects* **1850**, 861-871 (2015).
43. J. Huang *et al.*, CHARMM36m: an improved force field for folded and intrinsically disordered proteins. *Nature Methods* **14**, 71 (2016).
44. J. B. Klauda *et al.*, Update of the CHARMM All-Atom Additive Force Field for Lipids: Validation on Six Lipid Types. *The Journal of Physical Chemistry B* **114**, 7830-7843 (2010).
45. K. Vanommeslaeghe, A. D. MacKerell, Automation of the CHARMM general force field (CGenFF) I: Bond perception and atom typing. *Journal of Chemical Information and Modeling* **52**, 3144-3154 (2012).
46. T. Darden, D. York, L. Pedersen, Particle mesh Ewald: An N· log (N) method for Ewald sums in large systems. *J Chem Physics* **98**, 10089 (1993).
47. D.A. Case, D.S. Cerutti, T.E. Cheatham, III, T.A. Darden, R.E. Duke, T.J. Giese, H. Gohlke, A.W. Goetz, D. Greene, N. Homeyer, S. Izadi, A. Kovalenko, T.S. Lee, S. LeGrand, P. Li, C. Lin, J. Liu, T. Luchko, R. Luo, D. Mermelstein, K.M. Merz, G. Monard, H. Nguyen, I. Omelyan, A. Onufriev, F. Pan, R. Qi, D.R. Roe, A. Roitberg, C. Sagui, C.L. Simmerling, W.M. Botello-Smith, J. Swails, R.C. Walker, J. Wang, J. Wang, R.M. Wolf, X. Wu, L. Xiao, D.M. York and P.A. Kollman (2022), AMBER 2022, University of California, San Francisco.
48. Y. Miao, V. A. Feher, J. A. McCammon, Gaussian Accelerated Molecular Dynamics: Unconstrained Enhanced Sampling and Free Energy Calculation. *J Chem Theor Comput* **11**, 3584-3595 (2015).
49. J. Wang *et al.*, Gaussian accelerated molecular dynamics (GaMD): principles and applications. *Wiley Interdiscip Rev Comput Mol Sci* **11**, e1521 (2021).
50. D. R. Roe, T. E. Cheatham, 3rd, PTRAJ and CPPTRAJ: software for processing and analysis of molecular dynamics trajectory data. *J. Chem. Theory Comput.* **9**, 3084-3095 (2013).
51. Y. Miao *et al.*, Improved reweighting of accelerated molecular dynamics simulations for free energy calculation. *J. Chem. Theory Comput.* **10**, 2677-2689 (2014).
52. M. Ohi, Y. Li, Y. Cheng, T. Walz, Negative staining and image classification - powerful tools in modern electron microscopy. *Biol Proced Online* **6**, 23-34 (2004).
53. D. N. Mastronarde, Automated electron microscope tomography using robust prediction of specimen movements. *J Struct Biol* **152**, 36-51 (2005).
54. S. Q. Zheng *et al.*, MotionCor2: anisotropic correction of beam-induced motion for improved cryo-electron microscopy. *Nat Methods* **14**, 331-332 (2017).

55. A. Punjani, J. L. Rubinstein, D. J. Fleet, M. A. Brubaker, cryoSPARC: algorithms for rapid unsupervised cryo-EM structure determination. *Nat Methods* **14**, 290-296 (2017).
56. S. H. Scheres, RELION: implementation of a Bayesian approach to cryo-EM structure determination. *J Struct Biol* **180**, 519-530 (2012).
57. E. F. Pettersen *et al.*, UCSF Chimera--a visualization system for exploratory research and analysis. *J Comput Chem* **25**, 1605-1612 (2004).
58. T. Grant, A. Rohou, N. Grigorieff, cisTEM, user-friendly software for single-particle image processing. *Elife* **7**, (2018).
59. P. B. Rosenthal, R. Henderson, Optimal determination of particle orientation, absolute hand, and contrast loss in single-particle electron cryomicroscopy. *J Mol Biol* **333**, 721-745 (2003).
60. R. Sanchez-Garcia *et al.*, DeepEMhancer: a deep learning solution for cryo-EM volume post-processing. *Commun Biol* **4**, 874 (2021).
61. T. D. Goddard *et al.*, UCSF ChimeraX: Meeting modern challenges in visualization and analysis. *Protein Sci* **27**, 14-25 (2018).
62. T. I. Croll, ISOLDE: a physically realistic environment for model building into low-resolution electron-density maps. *Acta Crystallogr D Struct Biol* **74**, 519-530 (2018).
63. P. Emsley, K. Cowtan, Coot: model-building tools for molecular graphics. *Acta Crystallogr D Biol Crystallogr* **60**, 2126-2132 (2004).
64. P. V. Afonine *et al.*, Towards automated crystallographic structure refinement with phenix.refine. *Acta Crystallogr D Biol Crystallogr* **68**, 352-367 (2012).
65. H. Berman, K. Henrick, H. Nakamura, Announcing the worldwide Protein Data Bank. *Nat Struct Biol* **10**, 980 (2003).

Acknowledgements

We thank Drs. Christopher G. Tate and Javier García Nafría for providing the plasmid of mini-G399. We also thank Hiran Malinda Lamabadu Warnakulasurya and Natasha Jaiswal in assistance of GTP hydrolysis measurements. Dr. Hao Wu for technical assistance in cryo-EM data acquisition and advice on data processing and model building, Wooyoung Choi, Will Arnold and Adamo Mancino for their advice and feedback on figures, and to the members of the Cheng laboratory for helpful discussions. The cryo-EM facility at UCSF is managed by David Bulkley and Glenn Gilbert. Some of this work was performed at the Janelia cryo-EM facility, supported by Howard Hughes Medical Institute (HHMI). Computation at the Cheng laboratory is supported by Chengmin Li and Matt Harrington. This work is partly supported by grant from National Institute of Health (5R01GM132572(Y. M.), 5R35GM140847(Y.C.), and 1R01GM149659 (L. Y.)). Y.C. is also an investigator of Howard Hughes Medical Institute.

Author contributions

Conceptualization: LY

Methodology: MB, XD, JW, LY, YC, YM

Investigation: MB, XW, JW, JX, WS, VAA
Visualization: MB, XW, JW, LY
Funding acquisition: LY, YM, YC
Project administration: LY, YC
Supervision: LY, YM, YC
Writing-original draft: MB, YC, YM, LY
Writing-review & editing: MB, XW, JW, YM, YC, LY

Competing interests

The authors declare no competing financial interests.

Data Availability

The atomic coordinates of intermediate $A_{2A}R$-mini-$G\alpha_s\beta\gamma$ has been deposited in the Protein Data Bank with ID: 8VM3.

564 **Supplementary Materials**
565
566 **Materials and Methods**
567 **Plasmid construction and transformation**
568 The full-length human $A_{2A}R$ gene, originating from construct pPIC9K_ADORA2A, was
569 generously provided by Prof. Takuya Kobayashi (Kyoto University, Kyoto, Japan). The C-
570 terminally truncated construct $A_{2A}R$_316, constructed in our previous study, has an
571 integrated FLAG tag on the N-terminus and a poly-his tag on the C-terminus(*7*). Based
572 on this construct, the mutations V229C and R291A were described elsewhere(*13*). All
573 constructs were sequenced by a facility at Eurofins genomics, with the AOX1 primer pair
574 of PF_{AOX1} and PR_{AOX1}. Freshly prepared competent cells of strain *Pichia Pastoris* SMD
575 1163 (*Δhis4 Δpep4 Δprb1,* Invitrogen) were electro-transformed with *Pme*I-HF (New
576 England Biolabs) linearized plasmids containing different mutant genes using a Gene
577 Pulser II (Bio-Rad). High-copy clone selection was performed using an in-house protocol
578 described previously(*8, 34*). A high-yield construct was then screened by an
579 immunoblotting assay with both anti-FLAG and anti-Poly-his for further large-scale
580 expression screening.
581
582 **Receptor expression, purification, and labeling**
583 The screened WT* and mutants R291A, were pre-cultured on YPD [1% (w/v) yeast
584 extract, 2% (w/v) peptone and 2% (w/v) glucose] plates containing 0.1 mg/mL G418. A
585 single colony for each construct was inoculated into 4 mL YPD medium and cultured at
586 30 °C for 12 hours, then transferred into 200 mL BMGY medium [1% (w/v) yeast extract,
587 2% (w/v) peptone, 1.34% (w/v) YNB (yeast nitrogen base) without amino acids, 0.00004%
588 (w/v) biotin, 1% (w/v) glycerol, 0.1 M PB (phosphate buffer) at pH 6.5] and cultured at
589 30 °C for another 30 h. The cells were then transferred into 1 L of BMMY medium [1%
590 (w/v) yeast extract, 2% (w/v) peptone, 1.34% (w/v) YNB without amino acids, 0.00004%
591 (w/v) biotin, 0.5% (w/v) methanol, 0.1 M phosphate buffer at pH 6.5, 0.04% (w/v) histidine
592 and 3% (v/v) DMSO, 10 mM theophylline] at 20 °C. 0.5% (v/v) methanol was added every
593 12 h. 60 h after induction by methanol, cells were harvested for purification.
594
595 The cell pellets were collected by centrifugation at 4,000 ×g for 20 minutes and washed
596 one time with washing buffer (50 mM HEPES, 10% glycerol, pH 7.4) before the addition
597 of breaking buffer (50 mM HEPES, pH 7.4, 100 mM NaCl, 2.5 mM EDTA, 10% glycerol)
598 in a ratio of 4:1 (buffer: cells). The resuspended cell pellets were subject to disruption 3
599 times using a Microfluidizer at a pressure of 20,000 psi. Intact cells and cell debris were
600 separated by low-speed centrifugation (8,000 ×g) for 30 minutes. The supernatant was
601 collected and centrifuged at 100,000 ×g for 2 h, and the precipitated cell membrane was
602 then immediately dissolved in membrane lysis buffer (50 mM HEPES, pH 7.4, 100 mM
603 NaCl, 0.5% LMNG-3 (Lauryl Maltose Neopentyl Glycol) and 0.1% CHS (cholesteryl
604 hemisuccinate)) with rotation 2 h or overnight at 4 °C until the membrane was dissolved.
605 Subsequently, Talon resin (Clontech) was added to the solubilized membranes and
606 incubated for at least 2 h or overnight under gentle agitation.
607
608 The $A_{2A}R$-bound Talon resin was washed twice with a buffer of 50 mM HEPES, pH 7.4,
609 100 mM NaCl, 0.02% LMNG-3 and 0.002% CHS and resuspended in the same buffer.

610 The $A_{2A}R$-bound Talon resin was then resuspended in buffer made of 50 mM HEPES, pH
611 7.4, 100 mM NaCl, 0.02% LMNG-3 and 0.002% CHS, and combined with 10-20 fold
612 excess of the NMR label (2-bromo-*N*-(4-(trifluoromethyl)phenyl)acetamide, BTFMA,
613 Apollo Scientific, Stockport, UK) under gentle agitation overnight at 4 °C. Another aliquot
614 of NMR label was then added and incubated for an additional 6 h to ensure complete
615 labeling. The $A_{2A}R$-bound Talon resin was washed in a disposable column extensively
616 with buffer containing 50 mM HEPES, pH 7.4, 100 mM NaCl, 0.02% LMNG-3 and 0.01%
617 CHS, and apo $A_{2A}R$ was then eluted from the Talon resin with 50 mM HEPES, pH 7.4,
618 100 mM NaCl, 0.02% LMNG-3 and 0.01% CHS, 250 mM imidazole and concentrated to
619 a volume of 5 mL. The XAC-agarose gel and $A_{2A}R$ were then incubated together for 2 h
620 under gentle agitation. The functional $A_{2A}R$ was eluted with 50 mM HEPES, pH 7.4, 0.02%
621 LMNG-3, 0.002% CHS, 100 mM NaCl, 20 mM theophylline. The eluted samples were
622 concentrated to 1 mL by centrifugal filtration (MWCO, 3.5 KDa), and an extensive dialysis
623 was performed to remove the XAC in the sample. The functional apo $A_{2A}R$ was then
624 prepared for NMR. All receptors described in this manuscript were purified using poly-his
625 resin followed with a ligand-column, in which the $A_{2A}R$ antagonist xanthine amine
626 congener (XAC) was conjugated to Affi-Gel 10 activated affinity media.
627
628 **Preparation of mini-G$\alpha_s\beta\gamma$ heterotrimer**
629 The plasmid for mini-Gα_s399 was generously provided by Drs. Christopher G. Tate from
630 MRC Laboratory of Molecular Biology, Cambridge and Javier García Nafría from Institute
631 for Biocomputation and Physics of Complex Systems (BIFI) and Laboratorio de
632 Microscopías Avanzadas (LMA), University of Zaragoza. It was expressed in the *E. coli*
633 strain BL21(DE3). Cells were collected by centrifugation at 4,000 ×g for 20 min and lysed
634 by sonication. After another centrifugation, the supernatant was purified by Talon resin.
635 The sample was loaded into a HiLoad16/60 column to obtain purified mini-Gα_s protein.
636 The purified protein was concentrated to 3 mg/mL and flash frozen in liquid nitrogen and
637 stored at -80 °C for further use. The expression and purification of the respective
638 components and assembly to make the complex containing mini-G$\alpha_s\beta_1\gamma_2$, and the
639 preparation of nanobody Nb35, were all performed following the protocols described
640 previously (*1, 35, 36*).
641
642 **^{19}F NMR experiments**
643 NMR samples typically consisted of 280-300 μL volumes with 20-50 μM $A_{2A}R$ in 50 mM
644 HEPES buffer and 100 mM NaCl, doped with 10% D_2O. The receptor was stabilized in
645 0.02% LMNG-3 and 0.002% CHS. All ^{19}F NMR experiments were performed on a 600
646 MHz Varian Inova spectrometer using a ^{19}F dedicated resonance probe. Typical
647 experimental setup included a 16 μs 90° excitation pulse, an acquisition time of 200 ms,
648 a spectral width of 15 kHz, and a repetition time of 1 s. Most spectra were acquired with
649 15,000-50,000 scans. Processing typically involved zero filling, and exponential
650 apodization equivalent to 15 Hz line broadening.
651
652
653 **GTPase hydrolysis assay**
654 The GTPase hydrolysis assay was analyzed using a modified protocol of the GTPase-
655 Glo™ assay (Promega)(*37*). The reaction was started by mixing 300 nM G$\alpha_s\beta\gamma$ with the

656 purified receptors in varied concentrations with a final volume of 10 μL in the buffer
657 containing 50 mM HEPES, pH 7.4, 100 mM NaCl, 0.002% CHS, 0.02% LMNG-3. For the
658 GTP hydrolysis capacity of the S4 state as a function of ligand measurement, 5x and 25x
659 ligand compared to receptor concentration was added. After 30 min incubation at room
660 temperature, 10 μL 2xGTP-GAP solution containing 10 μM GTP, 1 mM DTT and the
661 cognate GAP was added to each well, followed with a 120 min incubation at room
662 temperature. For the Michaelis–Menten constant measurement, the 2xGTP-GAP solution
663 containing 5-50 μM GTP was used. Then, 20 μL reconstituted GTPase-Glo™ reagent
664 containing 5 μM ADP was added to each sample and incubated for another 30 min at
665 room temperature with shaking. Luminescence was measured following the addition of
666 40 μL detection reagent and incubation for 10 min at room temperature using a BioTEK-
667 Flx800 plate reader at 528±20 nm. Determine the amount of GTP consumed in a
668 biochemical reaction by referencing a standard curve that relates light units (RLU)
669 indicative of product formation to GTP concentration. Using this data, calculate the rate
670 of the enzymatic reaction (velocity, v) by applying the Michaelis-Menten equation: $v =$
671 $V_{max}/(1+(K_m/[S]))$. To facilitate the determination of V_{max} and K_m, construct a Lineweaver-
672 Burk plot, which linearizes the relationship by graphing the reciprocal of the velocity ($1/v$)
673 against the reciprocal of the substrate concentration ($1/[S]$). The calculations of initial
674 rates were performed at 1.08 min in the linear reaction phase of catalysis. Analysis of
675 data was performed by Excel and GraphPad Prism® 9.0.
676
677 **BODIPY-FL-GTP, BODIPY-FL-GDP binding, and nucleotide exchange**
678 The nucleotide-binding assay utilized BODIPY-FL-GTP and BODIPY-FL-GDP, from
679 Invitrogen™, each supplied as a mixture of two isomers with the fluorophore attached at
680 either the 2′ or 3′ position on the ribose ring. BODIPY-FL-GTP could be hydrolyzed to
681 BODIPY-FL-GDP. To form the GPCR-G protein complex, a solution containing 2 μM G
682 protein and 100 μM receptor was incubated for 30 minutes at 22°C. The fully activated
683 state of the WT* receptor was achieved by supplementing the mixture with 10 mM NECA.
684 Assays were conducted at 22°C using 96-well half-area microtiter plates in a BioTek plate
685 reader, with excitation at 475 nm and emission measured at 528 nm. The assay buffer
686 comprised 20 mM HEPES (pH 7.4), 1 mM EDTA, and 10 mM $MgCl_2$, supplemented with
687 0.01% LMNG-3 for protein stability. Initial kinetic data were acquired for 100 nM BODIPY-
688 FL-GTP/BODIPY-FL-GDP in the absence of G protein for 70 seconds to establish a
689 baseline fluorescence intensity. Subsequently, 200 nM heterotrimer G proteins, with or
690 without the receptor, were added, and mixing was rapidly performed in the fluorescence
691 cuvette. Data collection proceeded uninterrupted, and resulting kinetics spectra were
692 plotted and fitted to a one-phase association function using GraphPad Prism 9.0. For the
693 GTP-GDP exchange assay, the GPCR-G protein complex was formed as described,
694 followed by incubation with 100 nM BODIPY-FL-GDP for 2 hours. Baseline fluorescence
695 intensity was measured for 70 seconds using the plate reader, after which 1 μM GTP (in
696 a concentration of 10×GDP), procured from Invitrogen™, was added to facilitate the
697 exchange of BODIPY-FL-GDP to GTP. All experiments were repeated three times, and
698 resulting kinetics spectra were analyzed using GraphPad Prism 9.0.
699
700 **Gaussian accelerated molecular dynamics (GaMD)**

GaMD is an enhanced sampling method that works by adding a harmonic boost potential to reduce the system energy barriers (*38, 39*). When the system potential $V(\vec{r})$ is lower than a reference energy E, the modified potential $V^*(\vec{r})$ of the system is calculated as:

$$V^*(\vec{r})=V(\vec{r})+\Delta V(\vec{r})$$

$$\Delta V(\vec{r})=\begin{cases}\frac{1}{2}k\left(E-V(\vec{r})\right)^2, & V(\vec{r})<E\\ 0, & V(\vec{r})\geq E,\end{cases} \quad (1)$$

where *k* is the harmonic force constant. The two adjustable parameters E and k are automatically determined on three enhanced sampling principles. First, for any two arbitrary potential values $v_1(\vec{r})$ and $v_2(\vec{r})$ found on the original energy surface, if $V_1(\vec{r})<V_2(\vec{r})$, ΔV should be a monotonic function that does not change the relative order of the biased potential values; i.e., $V_1^*(\vec{r})<V_2^*(\vec{r})$. Second, if $V_1(\vec{r})<V_2(\vec{r})$, the potential difference observed on the smoothened energy surface should be smaller than that of the original; i.e., $V_2^*(\vec{r})-V_1^*(\vec{r})<V_2(\vec{r})-V_1(\vec{r})$. By combining the first two criteria and plugging in the formula of $V^*(\vec{r})$ and ΔV, we obtain

$$V_{max}\leq E\leq V_{min}+\frac{1}{k}, \quad (2)$$

Where V_{min} and V_{max} are the system minimum and maximum potential energies. To ensure that Eq. 2 is valid, *k* has to satisfy: $k\leq 1/(V_{max}-V_{min})$. Let us define: $k=k_0\cdot 1/(V_{max}-V_{min})$, then $0<k_0\leq 1$. Third, the standard deviation (SD) of ΔV needs to be small enough (i.e. narrow distribution) to ensure accurate reweighting using cumulant expansion to the second order: $\sigma_{\Delta V}=k(E-V_{avg})\sigma_V\leq\sigma_0$, where V_{avg} and σ_V are the average and SD of $\Delta V$with σ_0 as a user-specified upper limit (e.g., $10k_BT$) for accurate reweighting. When E is set to the lower bound $E=V_{max}$ according to Eq. 2, k_0 can be calculated as

$$k_0=\min\left(1.0,\ k_0'\right)=\min\left(1.0,\ \frac{\sigma_0}{\sigma_V}\cdot\frac{V_{max}-V_{min}}{V_{max}-V_{avg}}\right), \quad (3)$$

Alternatively, when the threshold energy E is set to its upper bound $E=V_{min}+1/k$, k_0 is set to:

$$k_0=k_0''\equiv\left(1-\frac{\sigma_0}{\sigma_V}\right)\cdot\frac{V_{max}-V_{min}}{V_{avg}-V_{min}}, \quad (4)$$

If $k_0''$is calculated between 0 and 1. Otherwise, k_0 is calculated using Eq. 3.

System setup and simulation analysis

The cryo-EM structure of wild-type NECA-bound $A_{2A}R$ bound by mini-$G\alpha_s$ (PDB ID: 6GDG(*16*)) was used for setting up simulation systems of the wild-type NECA-bound cWT*-$A_{2A}R$-mini-$G\alpha_s\beta\gamma$, *apo* cR291A-mini-$G\alpha_s\beta\gamma$, *apo* cWT*-$A_{2A}R$-$G\alpha_s\beta\gamma$ and *apo* cR291A-$G\alpha_s\beta\gamma$. The missing residues in the extracellular loop 2 (ECl2) and intracellular loop 3 (ICL3) of the receptor were modelled with Swiss-Modeller(*40*). For the *apo* cR291A-mini-$G\alpha_s\beta\gamma$, the simulation structure was generated by mutanting the correspoding R291A and V229C in the wild-type system and deleting the agonist NECA. To build the wild-type *apo* $A_{2A}R$ bound by the full-length of Gs protein (*apo* cWT*-$A_{2A}R$-$G\alpha_s\beta\gamma$), the Swiss-Modeller(*40*) was used to build the Gs protein with a geometry and orientation similar to the Gs protein in the fully active state of the β_2AR-Gs complex (PDB ID: 3SN6(*1*)). The coordinates of the GDP and Mg^{2+} were obtained by aligning the Ras domain of the crystal structure of Gs-bound GDP (PDB ID: 6AU6(*41*)) to the modelled

full-length Gs protein bound by the $A_{2A}R$.The simulation structure of the *apo* cR291A-$G\alpha_s\beta\gamma$ was generated by substituting residues Arg291 and Val232 in the wild-type system (*apo* cWT*-$A_{2A}R$-$G\alpha_s\beta\gamma$) with Ala and Cys, respectively.

VMD was used to insert the NECA-bound cWT*-$A_{2A}R$-mini-$G\alpha_s\beta\gamma$, *apo* cR291A-mini-$G\alpha_s\beta\gamma$, *apo* cWT*-$A_{2A}R$-$G\alpha_s\beta\gamma$, and *apo* cR291A-$G\alpha_s\beta\gamma$ complex into POPC (palmitoyl-2-oleoyl-sn-glycero-3-phosphocholine) lipids to prepare simulation systems. In each simulation system, the protein and lipid bilayer were solvated with TIP3P water molecules in a box of 11.2 nm x 13.1 nm x 14.6 nm with the periodic boundary condition. The system charge was neutralized with 150 mM NaCl. The CHARMM36m parameter set(*42-44*) was used for the proteins and lipids, and Guanosine diphosphate (GDP). Force field parameters of the NECA agonist were obtained from the ParamChem web server(*45*). The four simulation systems were first energy minimized for 5,000 steps with constraints on the heavy atoms of the proteins and phosphor atom of the lipids. The hydrogen-heavy atom bonds were constrained using the SHAKE algorithm and the simulation time step was set to 2.0 fs. The particle mesh Ewald (PME) method(*46*) was employed to compute the long-range electrostatic interactions and a cutoff value of 9.0 Å was applied to treat the non-bonded atomic interactions. The temperature was controlled using the Langevin thermostat with a collision frequency of 1.0 ps^{-1}. The system was then equilibrate using the constant number, volume, and temperature (NVT) ensemble at 310K for 250 ps and under the constant number, pressure, and temperature (NPT) ensemble at 310 K and 1 bar for another 1 ns with constraints on the heavy atoms of the protein, followed by 10 ns short conventional MD (cMD) without any constraint.

The GaMD module implemented in the GPU version of AMBER22(*47-49*) was then applied to perform the simulations of NECA-bound cWT*-$A_{2A}R$-mini-$G\alpha_s\beta\gamma$, *apo* cR291A-mini-$G\alpha_s\beta\gamma$, *apo* cWT*-$A_{2A}R$-$G\alpha_s\beta\gamma$, and *apo* cR291A-$G\alpha_s\beta\gamma$. GaMD simulations included a 8-ns short cMD run used to collect the potential statistics for calculating GaMD acceleration parameters, an 56-ns GaMD equilibration after adding the boost potential, and finally three independent 2,000-ns GaMD production simulations with randomized initial atomic velocities for the systems of the NECA-bound cWT*-$A_{2A}R$-mini-$G\alpha_s\beta\gamma$ and *apo* cR291A-$A_{2A}R$-mini-$G\alpha_s\beta\gamma$ complex, and 3,000-ns GaMD production simulations for the systems of *apo* cWT*-$A_{2A}R$-$G\alpha_s\beta\gamma$ and *apo* cR291A-$G\alpha_s\beta\gamma$ with randomized initial atomic velocities. The average and SD of the system potential energies were calculated every 800,000 steps (1.6 ns). All GaMD simulations were performed at the “dual-boost” level by setting the reference energy to the lower bound. One boost potential was applied to the dihedral energetic term and the other to the total potential energetic term. The upper limit of the boost potential SD, σ_0 was set to 6.0 kcal/mol for both the dihedral and the total potential energetic terms.

For each simulation system, all three GaMD production trajectories were combined together for analysis with CPPTRAJ(*50*). The distance between the NPxxY motif of the receptor and the last five residues of $G\alpha_s$ α5 helix ($A_{2A}AR$:NPxxY-$G\alpha_s$:α5 distance), the

distance between the receptor TM3 and TM6 intracellular ends (measured by the distance between the Cα atoms of receptor residues Arg102$^{3.50}$ and Glu228$^{6.30}$), the root-mean-square derivation of GDP (GDP RMSD) relative to the simulation starting structure were selected as reaction coordinates. The angle between the Ras domain and α helical domain (AHD) was used as another reaction coordinate to indicate their relative orientation, which was defined by the two vectors of $G\alpha_s$ AHD and $G\alpha_s$ Ras domain. Vector 1 went through the $G\alpha_s$ AHD and A161 centers and vector 2 went through $G\alpha_s$ Ras domain and E299 centers. The PyReweighting(*51*) toolkit was applied to reweight GaMD simulations to recover the original free energy profiles of the simulation systems. 2D free energy profiles were computed using the combined trajectories from all the three independent GaMD simulations for each system with the A_{2A}R:NPxxY-$G\alpha_s$:α5 distance, TM3-TM6 distance, GDP RMSD and the angle between the Ras domain and AHD as reaction coordinates. A bin size of 1.0 Å was used for the A_{2A}R:NPxxY-$G\alpha_s$:α5 distance, TM3-TM6 distance and GDP RMSD. A bin size of 6.0° was used for the angle between the Ras domain and AHD as reaction coordinate. The cutoff was set to 500 frames for 2D free energy calculations.

Preparation of the A_{2A}R-mini-$G_S\beta_1\gamma_2$-Nb35 complex

A_{2A}R, mini-G_S-$\beta_1\gamma_2$ and Nb35 were mixed in a molar ratio of 1:2:4, to yield a final complex concentration of 1 mg/mL. To this mixture, 0.1 U of apyrase was added, followed by an overnight incubation at 4°C. The mixture was then concentrated with a 100 kDa MWCO Amicon filter and injected onto a Superdex200 Increase 10/300 GL gel filtration column equilibrated with buffer (50 mM HEPES, 100 mM NaCl, 0.002% LMNG-3, 0.0002% CHS (w/v)). Monodisperse fractions were concentrated with a 100 kDa MWCO Amicon filter immediately prior to cryo-EM grid preparation.

Negative staining of the complex was performed with 0.75% uranium formate, following an established protocol(*52*).Grids were examined using an FEI T12 microscope operated at 120 kV, and images were recorded using a 4K x 4K charge-coupled device (CCD) camera (UltraScan 4000, Gatan).

Cryo-EM sample preparation and data acquisition

Freshly prepared A_{2A}R-mini-G_S-$\beta_1\gamma_2$-Nb35 complex at a final concentration of 1 mg/mL, was applied to glow-discharged gold grids coated with either holey carbon film (Quantifoil, 300 mesh 1.2/1.3, Au) or holey gold film (UltrAuFoil, 300, mesh 1.2/1.3). These grids were then plunge-frozen using a Vitrobot Mark IV with a blotting time of 4 s and blotting force of 0, at 4 °C and 100% humidity. Grids were subsequently examined and screened using an FEI Tecnai Arctica operated at 200 kV and equipped with an XFEG and a Gatan K3 camera. Cryo-EM data collection was performed on a Titan Krios at the UCSF Cryo-EM Center for Structural Biology, operated at an acceleration voltage of 300 kV, equipped with an XFEG, a BioQuantum energy filter (slit width set to 20 eV) and a K3 camera (Gatan).

All cryo-EM datasets were collected using SerialEM[(*53*)]. A multishot collection (3x3 arrays) was employed, incorporating beam-tilt compensation and maximum image shift is 3.5 micros. All images were acquired with a nominal magnification of 105 K, resulting in a

super-resolution pixel size of 0.4175 Å (physical pixel size of 0.835 Å). Defocus range was set from -0.8 µm to -1.8 µm. A total of 8,805 images were collected, each was dose-fractionated into 80 movie frames with a total exposure time of 2.024 s, resulting in a total fluence of approximately 47.7 electrons per $Å^2$. Data collection statistics are shown in Table S1.

Image process

A total of 8,805 movie stacks were motion-corrected, dose-weighted, and binned by Fourier cropping to the physical pixel size of 0.835 Å on-the-fly using MotionCor2[54]. Motion-corrected, does-weighted sums were used for contrast transfer function (CTF) determination and resolution estimation in cryoSPARC[55]. 424,536 particles were picked from randomly selected 500 micrographs using cryoSPARC blob picker with a diameter of 80-150 Å. These particles were subjected to ab-initio reconstruction and multi-round heterogenous refinement. One class with distinct features of $A_{2A}R$ bound to mini-$G\alpha_s\beta_1\gamma_2$-Nb35 was identified, from which 16 different projection images were created for template picking, yielding 7,282,317 particles from all micrographs.

After removing junk particles by extensive 2D classifications, 2,328,810 particles were selected for ab-initio reconstruction and multi-round heterogenous refinement. One distinct class of 307,568 particles was identified for further non-uniform refinement of the $A_{2A}R$-mini-$G\alpha_s\beta_1\gamma_2$-Nb35 complex, yielding a reconstruction with a global resolution of 3.04Å. This particle stack was then exported to RELION[56] for multiple rounds of 3D refinement (initial low-pass filter: 10 Å; mask diameter: 360 Å; reference mask: no) to produce a new reconstruction, from which a mask without the detergent micelle was generated by using the segment map function in Chimera[57] (initial threshold: 0.0001; extend_inimask: 4; width_soft_edge: 4). Particle subtraction function in RELION was applied by using this mask to generate a micelle removed particle stack.

Next, we applied 3D classification to the micelle subtracted particles with a reference model without micelle (reference mask: generated last step; initial low-pass filter: 10 Å; mask diameter: 260 Å; regularisation parameter T: 3; number of iterations: 50; number of classes: 5; perform local angular searches: no). A new reconstruction of the entire $A_{2A}R$-mini-G_S-$\beta_1\gamma_2$-Nb35 complex from 71,547 particles was identified for further refinement in RELION (initial low-pass filter: 3.5 Å; mask diameter: 260 Å; angular sampling interval: 1.8º; local search from auto-sampling: 0.9º). A final 3D reconstruction was calculated in cisTEM[58] with default settings and without further refinement. The numeric resolution was determined from Fourier Shell Correction (FSC) using criterion of FSC = 0.143[59]. The final map was sharpened by DeepEMhancer[60] and used for model building and figure generation.

Model building

For model building, the initial model was generated by fitting the existing coordinates of the activated state of $A_{2A}R$-mini-G_S-$\beta_1\gamma_2$-Nb35 complex (PDB: 6GDG) into our cryo-EM density maps using ChimeraX[61]. Discrepancies between the initial model and the density maps were then manually built and refined ISOLDE(*62*) and coot[63]. Subsequent refinements were performed in Phenix[64] with secondary structure constraints. The model

was validated by wwPDB validation server(*65*) and no major issues was reported. A summary of the parameters used in data collection and model building is provided in Table S1.

Data representation

All statistical tests such as GTP hydrolysis assessments were conducted using GraphPad Prism 9.0. The central point of all data points gives the mean value with s.d. for all data unless otherwise specified. Visualization of the atomic models (figures and videos) were made using UCSF ChimeraX and PyMoL (The PyMOL Molecular Graphics System, Version 2.0 Schrödinger, LLC.)

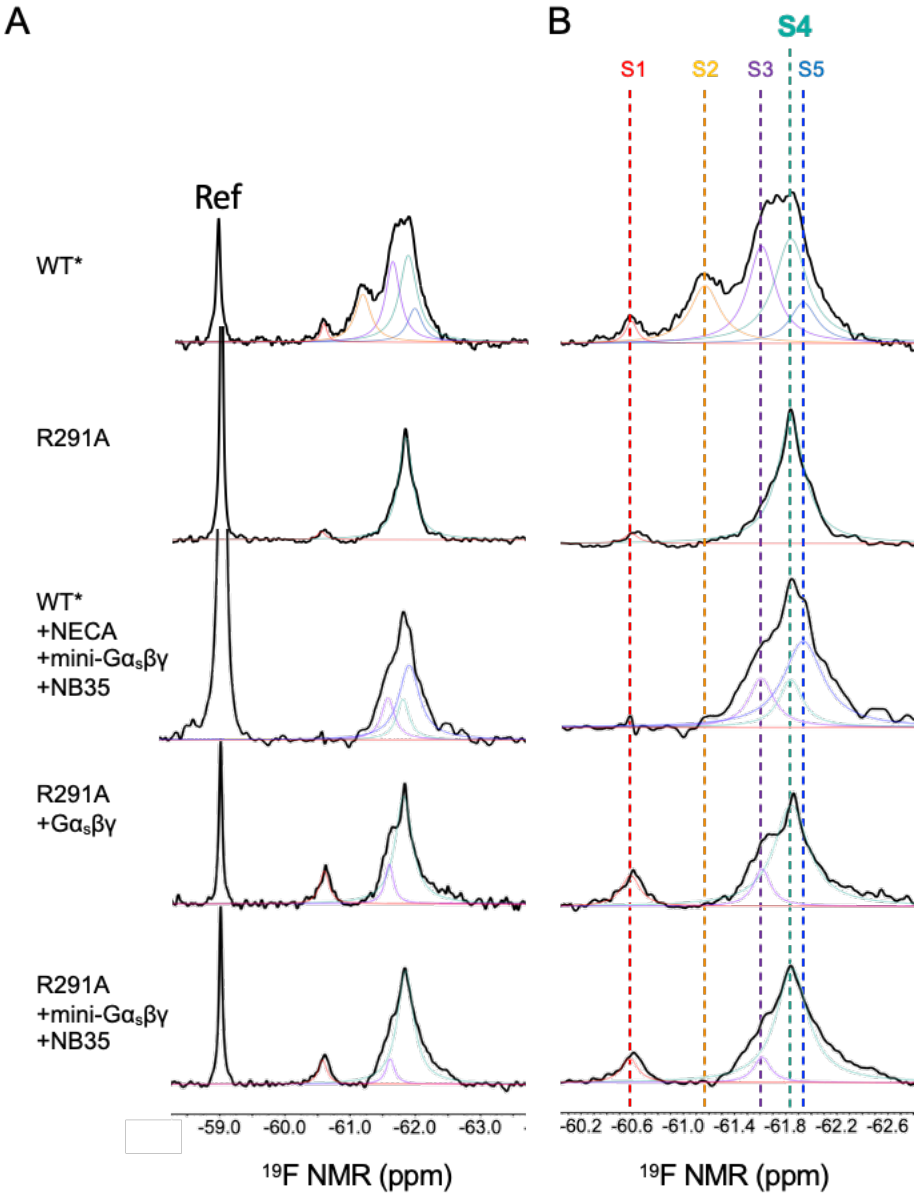

Fig. S1. Conformational profiles of the mutant R291A and its complexes probed by ^{19}F-qNMR. (A) and **(B),** Deconvoluted conformational profiles probed by ^{19}F-qNMR as a function of mini-Gαsβγ and Gαsβγ (S4-Gαβγ), in reference to the WT*-mini-Gαsβγ+NB35 (S5-Gαsβγ), representing the conformational profile for the structure PDB ID: 6GDG.

895
896
897
898

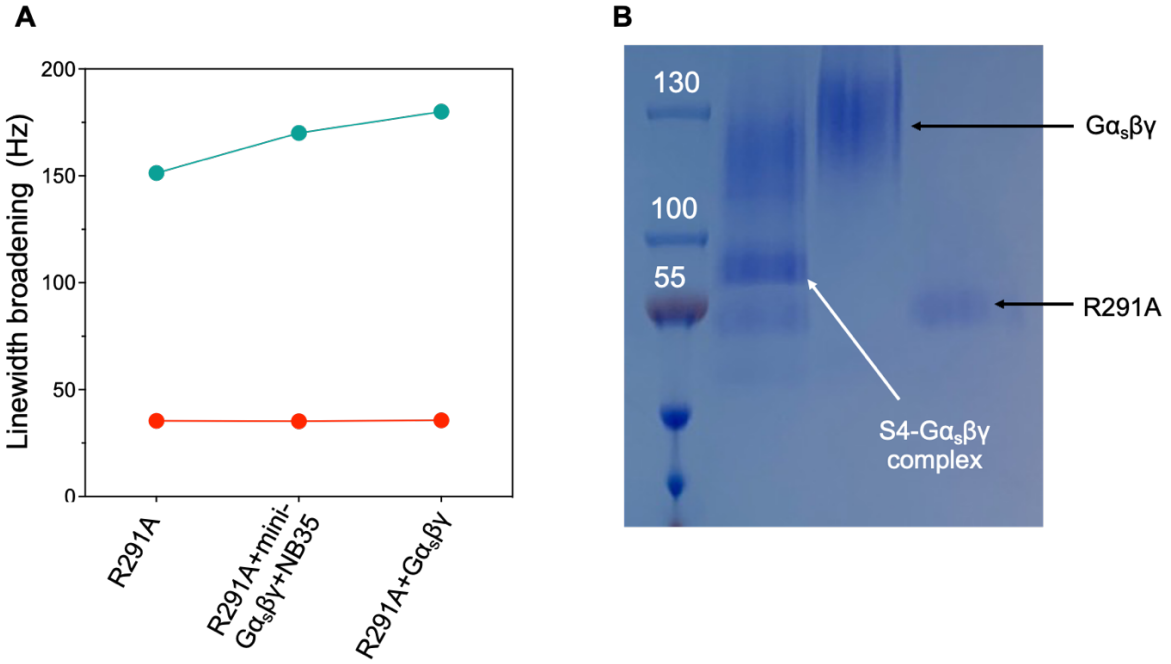

Fig. S2. Both linewidth broadening of ^{19}F-qNMR resonance for S4 intermediate and native-PAGE indicated the complex formation between the S4 and G protein. (A) Linewidths of S4 resonance for R291A, R291A-G$\alpha_s\beta\gamma$, and R291A-mini-G$\alpha_s\beta\gamma$-NB35. **(B)** Native-PAGE for R291A and G$\alpha_s\beta\gamma$ interaction.

899
900
901
902
903
904
905
906
907
908

909

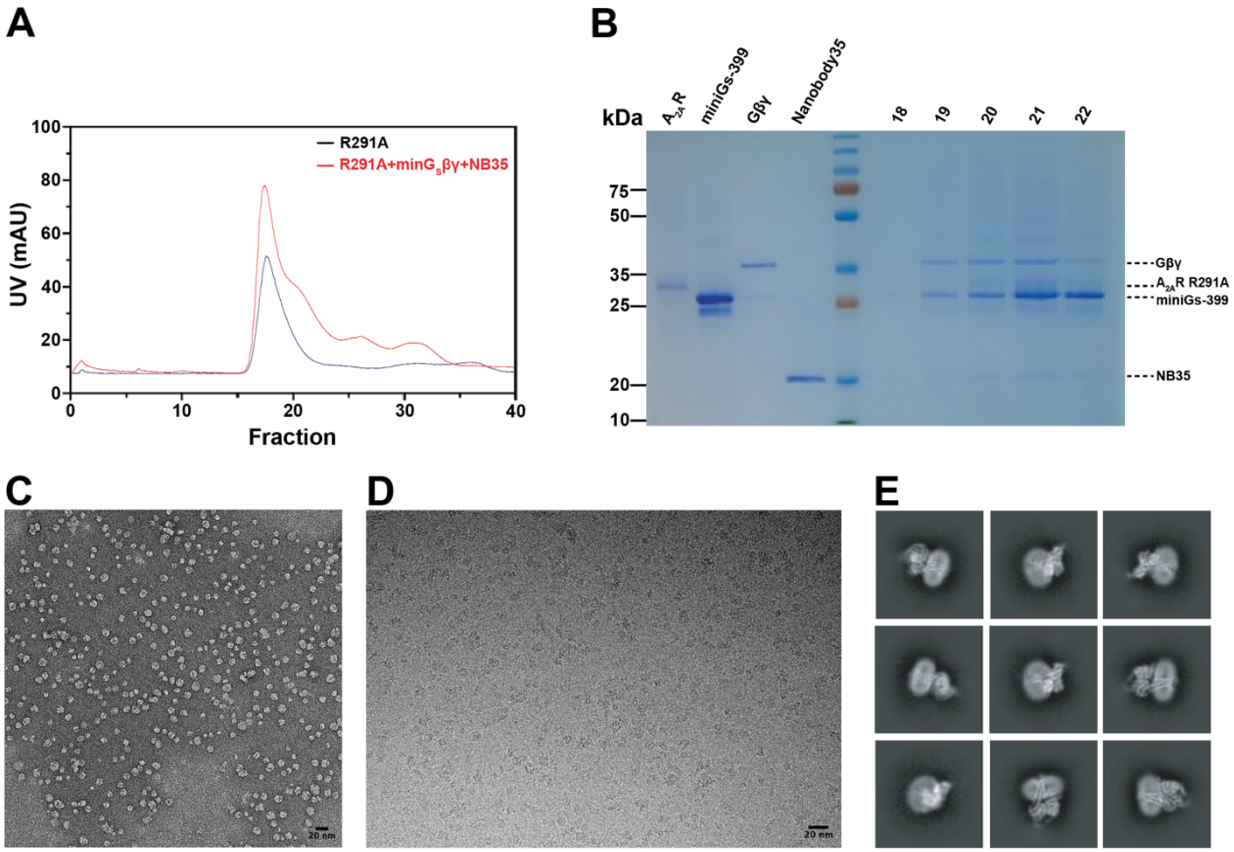

Fig. S3. Preparation of $A_{2A}R$ sample and cryo-EM screening. (A) Size exclusion chromatography of purified $A_{2A}R$-R291A with and without mini-$G_s\beta\gamma$+NB35. **(B)** SDS-PAGE of the indicated fraction, corresponding to R291A+mini-$G\alpha_s\beta\gamma$+NB35. **(C)** Negative staining of the R291A+ mini-$G\alpha_s\beta\gamma$+NB35 complex. **(D)** Representative cryo-EM micrograph of the complex. **(E)** Representative 2D average image of the complex.

910
911
912
913
914
915

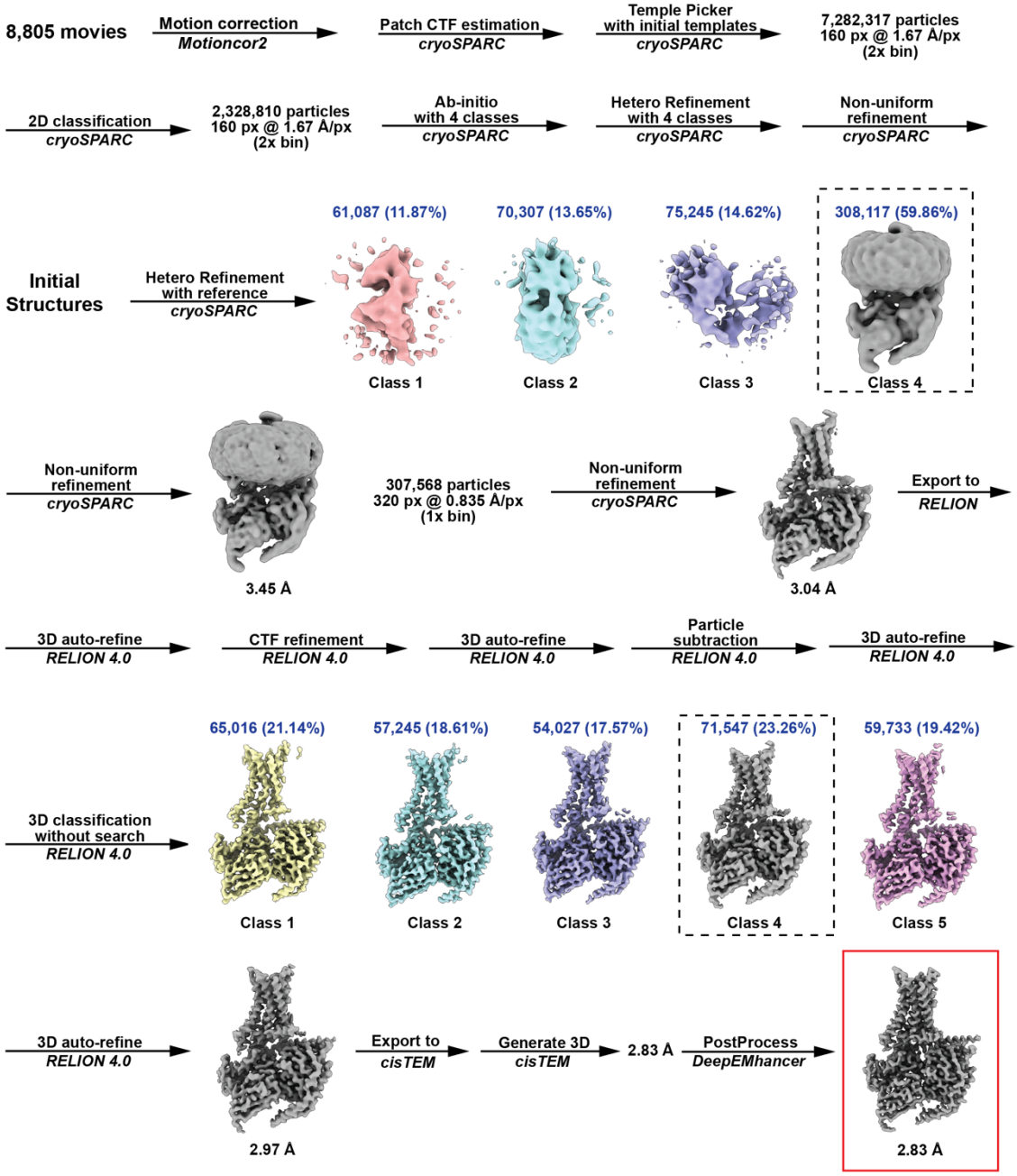

Fig. S4. Cryo-EM data and image processing flow. Schematic flow-chat representing the image processing approach for A_{2A}R-R291A. Thumbnail images of each 3D class or refinement are shown along with global GS-FSC resolution in black, particles counts in blue, and dashed black boxes to indicate selected 3D classes. Cryo-EM map (red box) and atomic model are used in main figures to present A_{2A}R-R291A features.

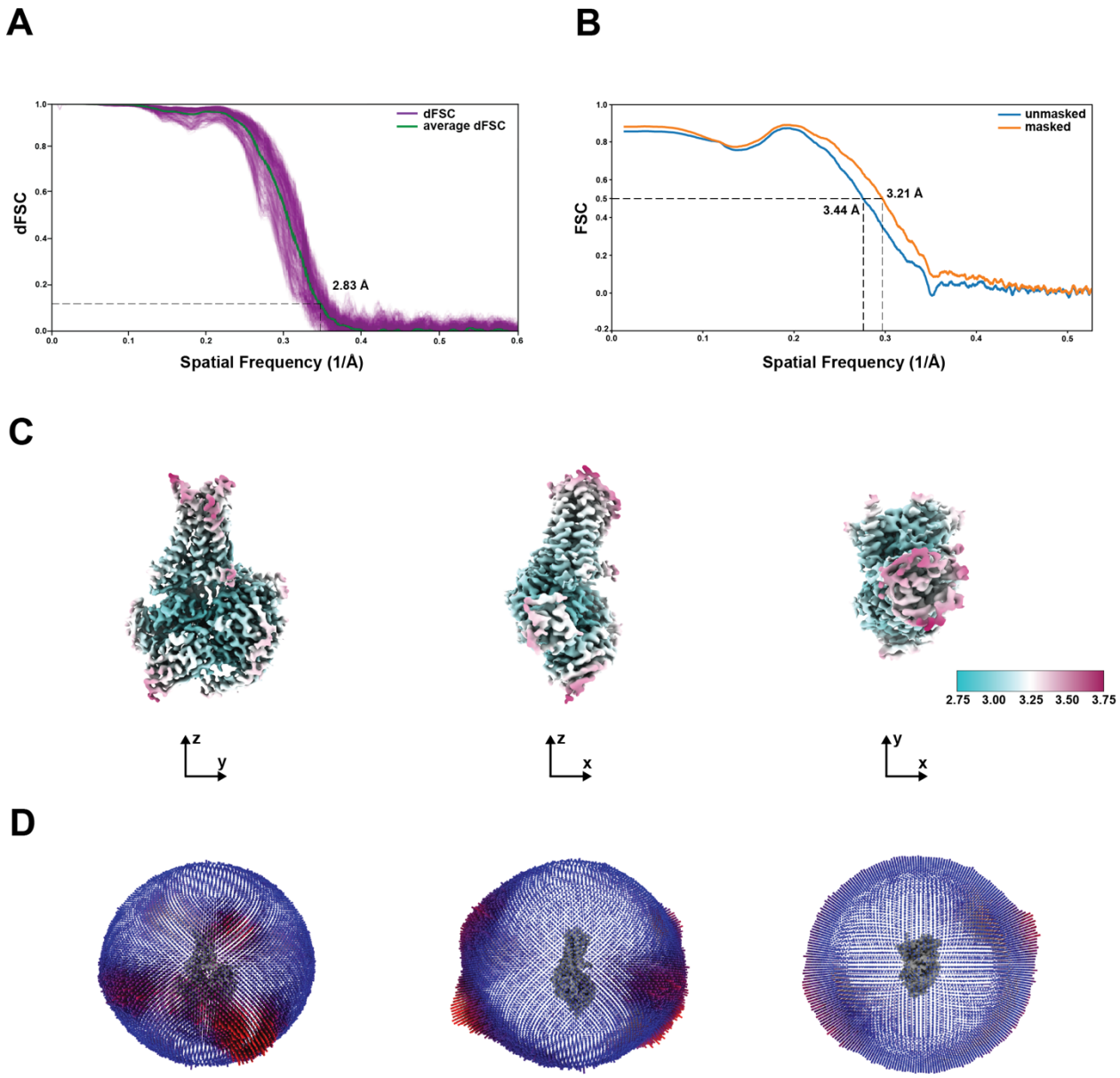

Fig. S5. Resolution estimation and atomic model quality. (A) Fourier shell correlation curve with resolution determined by the 'gold-standard' FSC. **(B)** Model-to-map FSC plots calculated by PHENIX between the map and the model. **(C)** Cryo-EM map colored by local resolution estimates using RELION with resolution scale bar (Å). **(D)** Histogram representation of the Euler angle distribution from the final particles used in the reconstruction.

926

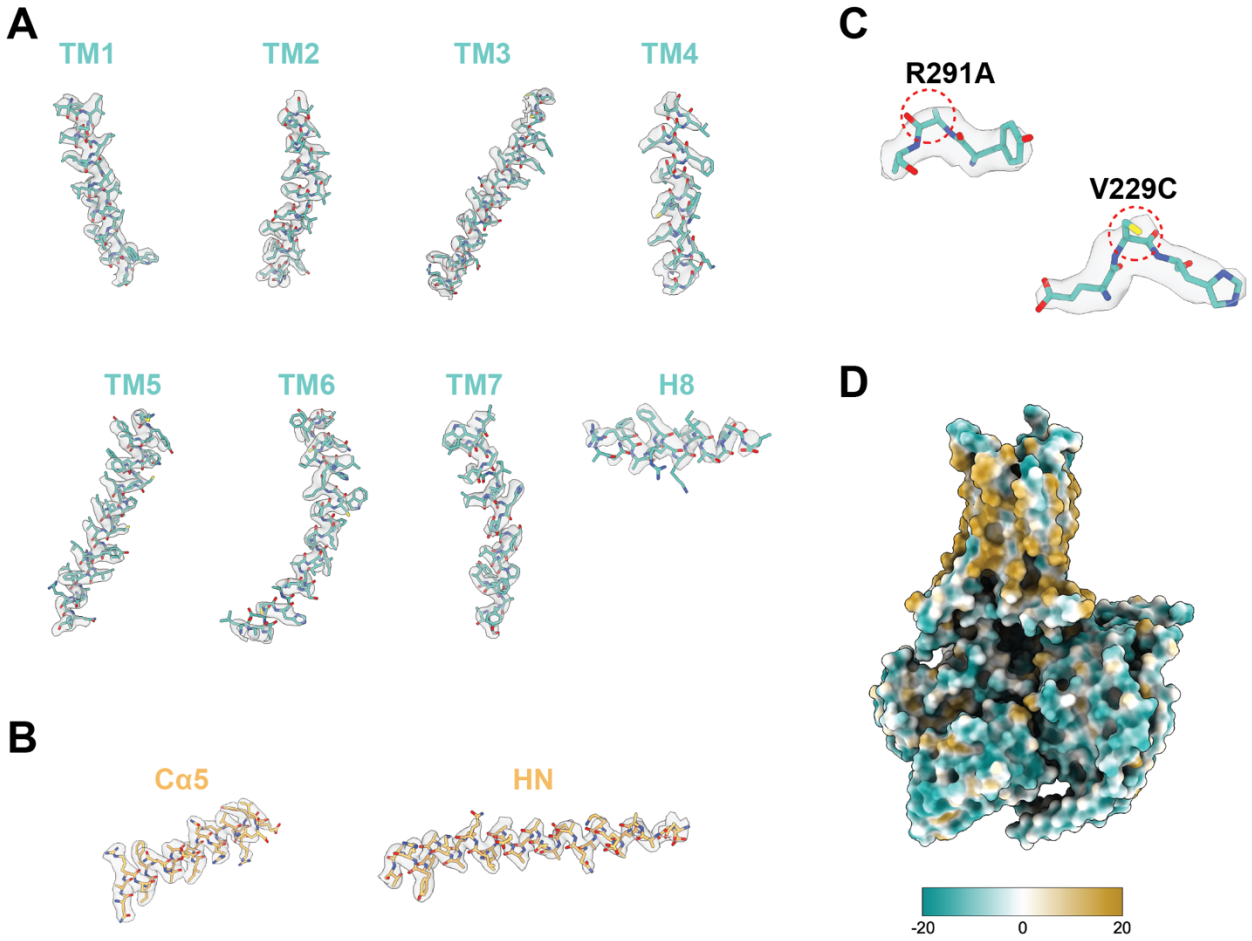

Fig. S6. Representative cryo-EM densities from selected structural features of $A_{2A}R$. (A) Densities of all transmembrane helices. **(B)** Representative densities of mini-G. **(C)** Cryo-EM densities of V229C and R291A. **(D)** Representation of surface hydrophobicity.

927
928
929
930
931
932
933

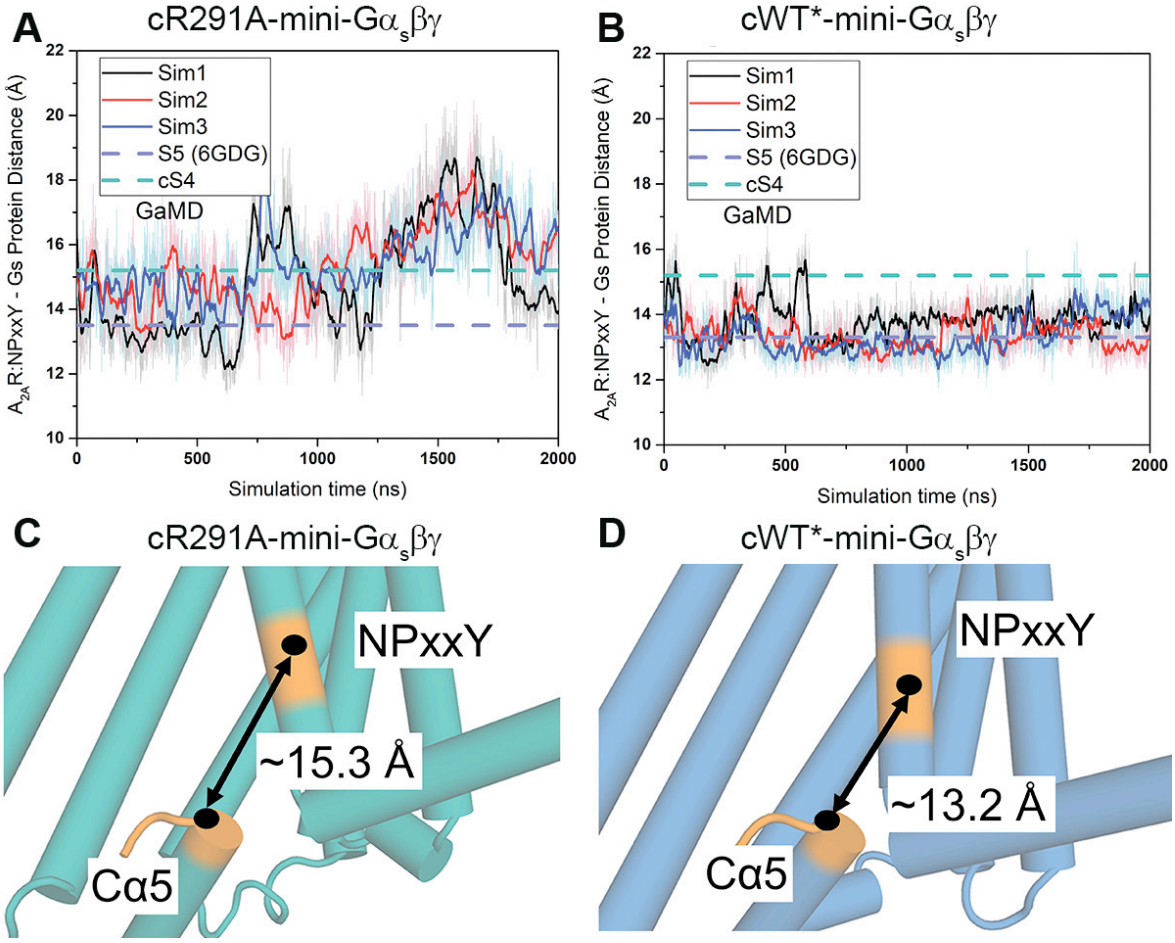

Fig. S7. GaMD simulations for cR291A-mini-Gα$_s$βγ and cWT*-mini-Gα$_s$βγ. (A-B), Time course of the center-of-mass (COM) distance between the receptor NPxxY motif in TM7 and the Cα5 helix (A_{2A}R:NPxxY-Gαs:Cα5 distance) calculated from the GaMD simulations of cR291A-mini-Gα$_s$βγ (**A**) and cWT*-mini-Gα$_s$βγ (**B**) complex systems. **(C-D)**, Representative low-energy conformations of the cR291A-mini-Gα$_s$βγ (**C**) and **(D)** cWT*-mini-Gα$_s$βγ complex identified from the GaMD simulations. The receptor NPxxY motif and the last five residues of Gα5 helix were colored in orange.

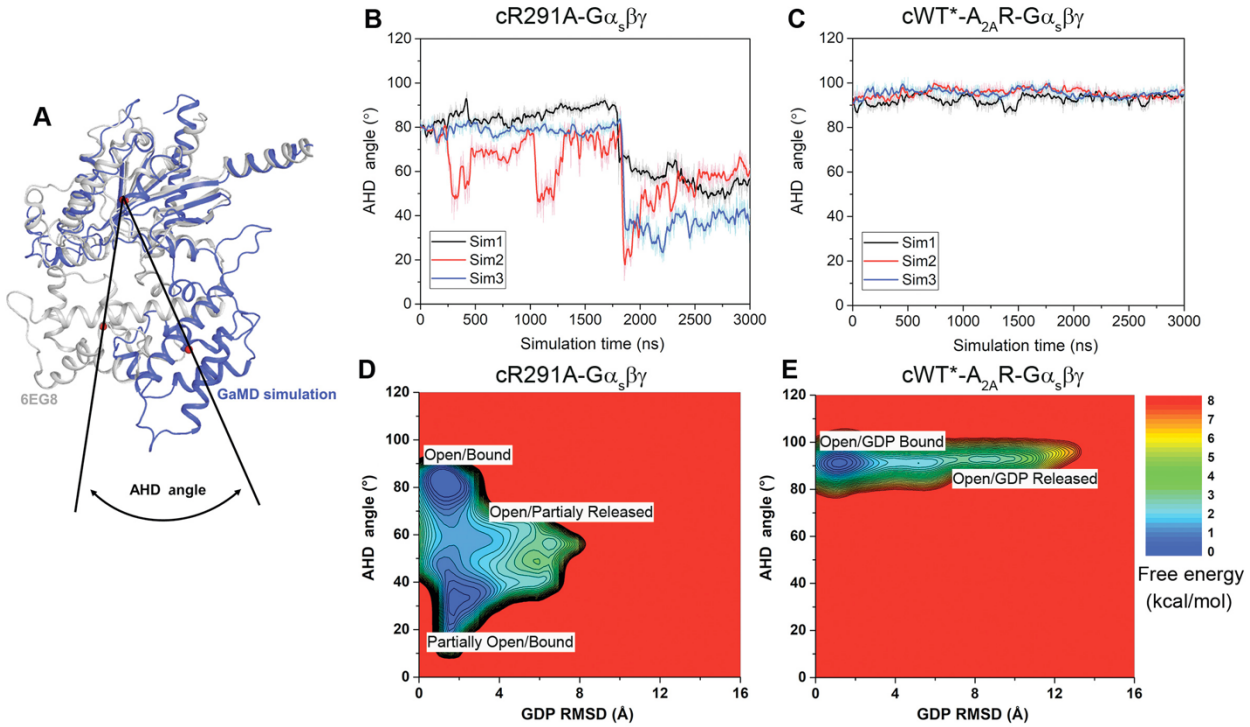

Fig. S8. The behaviors of AHD domain. (A) The AHD angle is illustrated by comparing the GaMD simulation conformation with the inactive conformation of $G\alpha_s$ (PDB: 6EG8); Vector 1 goes through centers of the $G\alpha_s$ AHD and Ras-like domain of the inactive conformation (6EG8). Vector 2 goes through the centers of the $G\alpha_s$ AHD and Ras-like domain of the GaMD simulation conformations after aligning the Ras-like domain to the inactive conformation of $G\alpha_s$. **(B-C)**, The time course of the AHD angle calculated from the GaMD simulations for the *apo* cR291A-$G\alpha_s\beta\gamma$ (**B**) and *apo* cWT*-A_{2A}R-$G\alpha_s\beta\gamma$ (**C**) complexes. **(D-E)** 2D free energy profiles of the *apo* cR291A-$G\alpha_s\beta\gamma$ (**D**) and *apo* cWT*-$G\alpha_s\beta\gamma$ (**E**) complexes calculated from GaMD simulations regarding the GDP RMSD and the AHD angle.